Icarus 335 (2020) 113395

Contents lists available at ScienceDirect

Icarus

journal homepage: www.elsevier.com/locate/icarus

Cosmic dust fluxes in the atmospheres of Earth, Mars, and Venus

Juan Diego Carrillo-Sánchez[a], Juan Carlos Gómez-Martín[b], David L. Bones[a], David Nesvorný[c], Petr Pokorný[d,e], Mehdi Benna[e,f], George J. Flynn[g], John M.C. Plane[a,*]

[a] School of Chemistry, University of Leeds, Woodhouse Lane, Leeds LS2 9JT, UK,
[b] Instituto de Astrofísica de Andalucía (IAA-CSIC), 18008 Granada, Spain,
[c] Southwest Research Institute, Department of Spaces Studies, 050 Walnut St. Boulder, CO 80302, USA
[d] The Catholic University of America, Department of Physics, 620 Michigan Ave., Washington, DC 20064, USA
[e] NASA Goddard Space Flight Center, Solar System Exploration Division, 8800 Greenbelt Rd., Greenbelt, MD, USA
[f] University of Maryland Baltimore County, 1000 Hilltop Circle, Baltimore, MD 21250, USA
[g] State University of New York at Plattsburgh, Department of Physics, 101 Broad Street, Plattsburg, NY 12901, USA

A B S T R A C T

The ablation of cosmic dust injects a range of metals into planetary upper atmospheres. In addition, dust particles which survive atmospheric entry can be an important source of organic material at a planetary surface. In this study the contribution of metals and organics from three cosmic dust sources – Jupiter-Family comets (JFCs), the Asteroid belt (AST), and Halley-Type comets (HTCs) – to the atmospheres of Earth, Mars and Venus is estimated by combining a Chemical Ablation Model (CABMOD) with a Zodiacal Cloud Model (ZoDy). ZoDy provides the mass, velocity, and radiant distributions for JFC, AST, and HTC particles. JFCs are shown to be the main mass contributor in all three atmospheres (68% for Venus, 70% Earth, and 52% for Mars), providing a total input mass for Venus, Earth and Mars of $31 \pm 18\,t\,d^{-1}$, $28 \pm 16\,t\,d^{-1}$ and $2 \pm 1\,t\,d^{-1}$, respectively. The mass contribution of AST particles increases with heliocentric distance (6% for Venus, 9% for Earth, and 14% for Mars). A novel multiphase treatment in CABMOD, tested experimentally in a Meteoric Ablation Simulator, is implemented to quantify atmospheric ablation from both the silicate melt and Fe-Ni metal domains. The ratio of Fe:Ni ablation fluxes at Earth, Mars and Venus are predicted to be close to their CI chondritic ratio of 18, in agreement with mass spectrometric measurements of Fe^+:$Ni^+ = 20^{+13}_{-8}$ in the terrestrial ionosphere. In contrast, lidar measurements of the neutral atoms at Earth indicate Fe:Ni = 38 ± 11, and observations by the Neutral Gas and Ion Mass Spectrometer on the MAVEN spacecraft at Mars indicate Fe^+:$Ni^+ = 43^{+13}_{-10}$. Given the slower average entry velocity of cosmic dust particles at Mars, the accretion rate of unmelted particles in Mars represents 60% of the total input mass, of which a significant fraction of the total unmelted mass (22%) does not reach an organic pyrolysis temperature (~900 K), leading to a flux of intact carbon of $14\,kg\,d^{-1}$. This is significantly smaller than previous estimates.

1. Introduction

Knowing the magnitude of the mass influx of Interplanetary Dust Particles (IDPs) into a solar system body is crucial for understanding the impacts in the atmosphere and at the surface. Astronomical dust models are therefore required to characterize the production, evolution and transport of dust grains from their sources to the planetary atmosphere. These models predict the dust velocity and mass distributions, as well as the radiants of meteor showers and the sporadic background. Depending on these three parameters – mass, velocity, and radiant - dust grains can fully ablate on atmospheric entry, or survive either as an unmelted micrometeorite (if the dust particle does not reach the melting temperature) or as a cosmic spherule (partially or completely metamorphosed at temperatures higher than the melting point) (Carrillo-Sánchez et al., 2016; Carrillo-Sánchez et al., 2015).

Meteoric ablation produces layers of free neutral and ionized atoms in a planetary atmosphere. Mg, Fe, Na and Si are the most abundant metallic species in the Earth's upper atmosphere, with K and Ca at least one order of magnitude lower in concentration (Plane, 2003). Meteor showers may increase the concentration of metals by a factor of 2–3 during a discrete time period, but represent probably < 10% of the annual mass input to the terrestrial atmosphere. The impact of showers is therefore difficult to detect in the metal layers (Grebowsky et al., 1998; Kopp, 1997), although an enhancement in lower *E* region ionization was reported during the 2002 Leonid shower (Pellinen-Wannberg et al., 2014). Although the metallic layers in the Earth's atmosphere have been studied for decades using ground-based lidar and space-based optical spectroscopy (Plane et al., 2015), the first measurements in another planetary atmosphere were only made very recently: a persistent layer of Mg^+ peaking around 90 km was detected in Mars' atmosphere by the Imaging Ultraviolet Spectrograph (IUVS) on board the Mars Atmosphere and Volatile Evolution (MAVEN) spacecraft (Crismani et al., 2017). A range of metallic ions has also been measured using the Neutral Gas Ion Mass Spectrometer (NGIMS) on MAVEN,

* Corresponding author.
E-mail address: j.m.c.plane@leeds.ac.uk (J.M.C. Plane).

https://doi.org/10.1016/j.icarus.2019.113395
Received 10 March 2019; Received in revised form 30 May 2019; Accepted 29 July 2019
Available online 02 August 2019

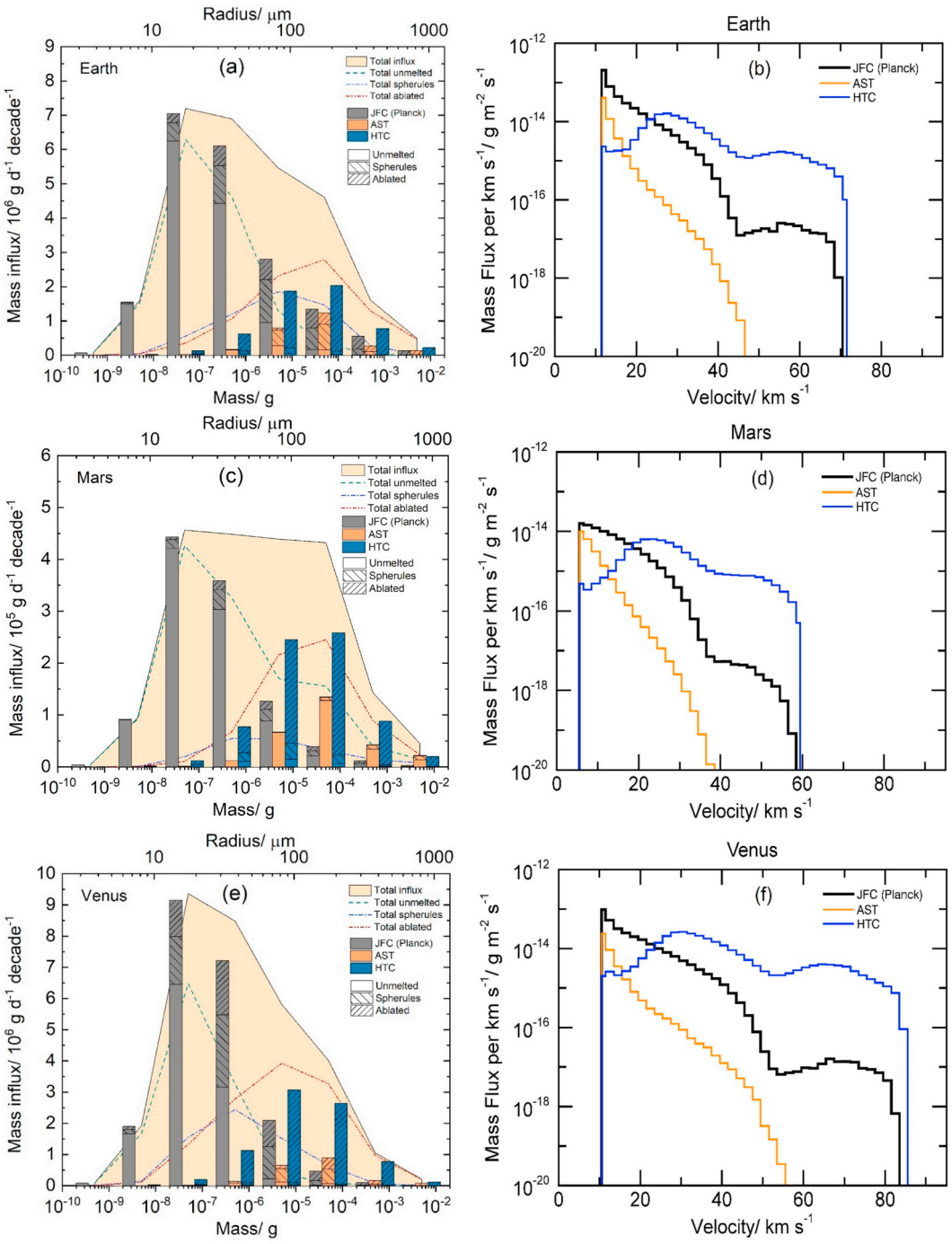

Fig. 1. (a), (c) and (e): Histograms displaying the mass influx rate into the atmospheres of Earth, Mars, and Venus over the mass range considered by the Zodiacal Cloud Model for particles from Jupiter Family Comets (dark-grey), the Asteroid belt (orange), and Halley Type Comets (blue). The JFC results are constrained with the Planck observations. The total mass influx for each cosmic dust source is also partitioned into surviving particles – unmelted mass (unshaded) and spherules (shaded with left-slanting lines) – and total ablated mass (shaded with right-slanting lines). The overall fluxes are represented by lines: total (solid black), unmelted (green dashed), spherules (blue dot-dashed), and ablated (red dot-dashed). (b), (d) and (f): the mass influx as a function of entry velocity for these three cosmic dust populations. (For interpretation of the references to color in this figure legend, the reader is referred to the web version of this article.)

during deep-dip orbits down to ~130 km (Grebowsky et al., 2017). Schneider et al. (2015) and Benna et al. (2015b) also reported the detection of metallic ion layers produced by the meteor storm event following the close encounter between Comet Siding Spring (C/2013 A1) and Mars. Currently, all the information about metallic species in Venus' atmosphere is indirect: the radio occultation technique was used with Pioneer Venus (Kliore et al., 1979) and Venus Express (Paetzold et al., 2009) to show that a secondary ion layer occurs around 115–120 km, which is close to the meteoric ablation altitude (see below), and is ~22 km below the main ion layer. Based on our knowledge from the terrestrial atmosphere, the neutral metal atom layers occur below the metal ion layers (Plane et al., 2015), and the metals are partitioned between atoms and ions through a photochemical steady state which favours ions at higher altitudes. Metal atoms may undergo collisional ionization during ablation, or subsequently through photo-ionization and charge transfer reactions with the

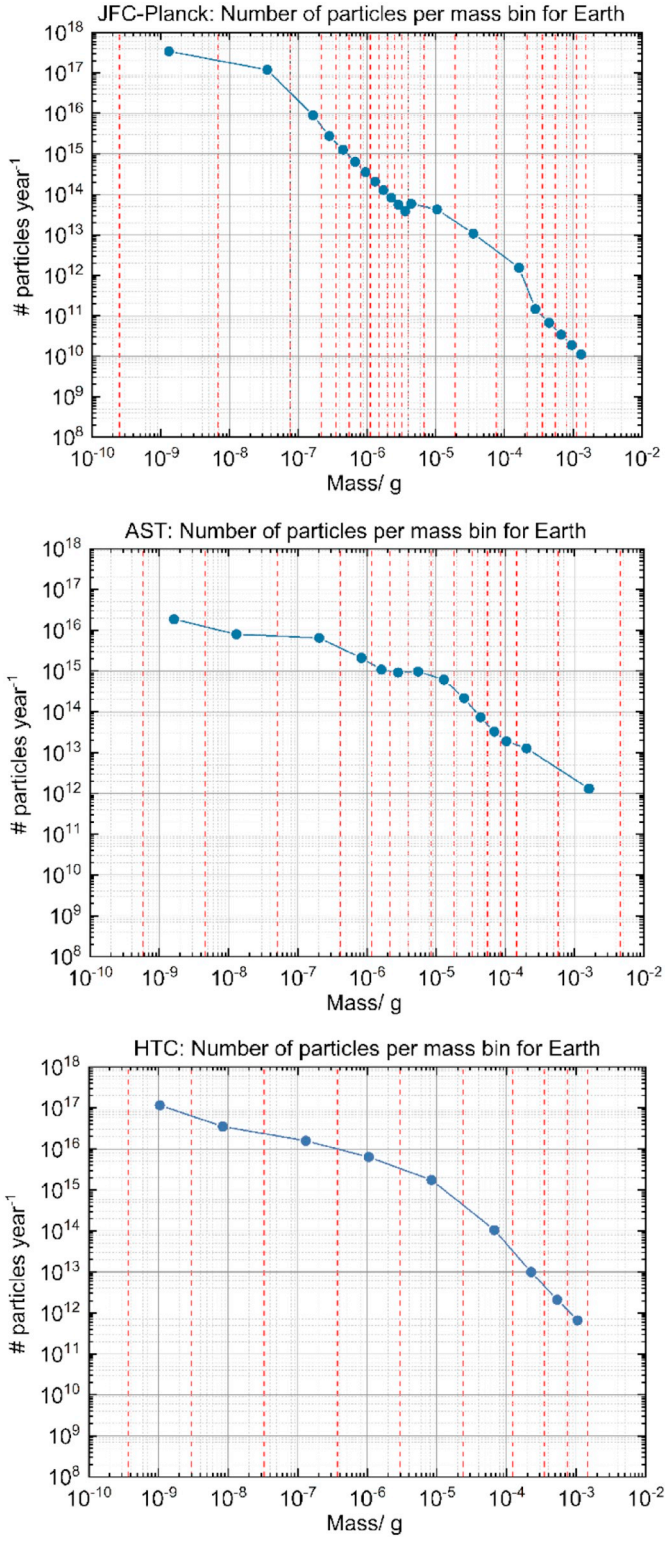

Fig. 2. Mass distributions of JFC-Planck, AST, and HTC particles for Earth. Each blue point is the mass taken from the ZoDy model. The red-dashed lines represent the delimiters between two consecutive mass bins and are characterized as the geometric mean of the diameters of these two masses, assuming a particle density of 2.2 g cm^{-3} (Consolmagno et al., 2008). Each pair of delimiters defines the width of a given mass bin. (For interpretation of the references to color in this figure legend, the reader is referred to the web version of this article.)

major lower ionospheric ions, such as NO^+ and O_2^+ on Earth (Plane, 2003; Plane et al., 2015) and O_2^+ on Mars (Whalley and Plane, 2010). The metal ions in turn form molecular cluster ions, which then undergo dissociative recombination with electrons to reform metal atoms. The time-scales of atom-ion interconversion tend to be rapid compared with the timescale of vertical transport. Therefore, in the discussion in the following sections we treat metal ions and atoms interchangeably.

Carrillo-Sánchez et al. (2016) constrained the mass contribution at Earth from four known cosmic dust sources: Jupiter-Family Comets (JFCs), Asteroid belt (ASTs), Halley-Type Comets (HTCs) and Oort-Cloud Comets (OCCs). The measured vertical fluxes of Na and Fe atoms in the Earth's upper mesosphere, and the rate of cosmic spherule deposition at the surface were used to show that the total mass input was 43 ± 14 t d^{-1} (tonnes per Earth day), with the major contribution of (80 ± 17)% from JFCs. More recently, Borin et al. (2017) determined a mass input of 15.3 ± 2.6 t d^{-1} from an astronomical dust model numerically integrating asteroidal dust particles.

In the case of Mars, Flynn and McKay (1990) determined a global dust input rate of 7.4–161.5 t d^{-1} (for particles in the mass range 10^{-7} - 10^{-3} g, about 30–600 μm in radius). This estimate was obtained by extrapolating the flux at Earth, and taking into account crater impacts in the Martian surface along with the dynamical evolution of particles close to Mars' orbit. More recently, the Langmuir Probe and Waves (LPW) instrument on MAVEN constrained the mass flux of dust particles at Mars to between 0.086 and 8.6 t d^{-1} (Andersson et al., 2015), although the analysis was done for a narrow mass range of 10^{-11} - 8×10^{-8} g (1–12 μm in radius). Likewise, the extrapolation of MAVEN/IUVS observations of Mg^+ suggests an overall mass influx of 2 – 3 t d^{-1} (Crismani et al., 2017). The recent modelling study of Borin et al. (2017) estimated an input of 8.1 ± 0.6 t d^{-1}. For Venus, this study found an input of rate of 18.9 ± 1.5 t d^{-1}.

In the present study, we focus on meteoric ablation in the atmospheres of Earth, Mars, and Venus. For this purpose, we use the new version of the Chemical Ablation MODel (CABMOD) which has been recently updated with a multiphase treatment to account for the ablation of both bulk silicate and the Fe-Ni metal grains which are normally present in IDPs (Bones et al., 2019). This new version of CABMOD is then combined with the Zodiacal Cloud Model (ZoDy) (Nesvorný et al., 2011; Nesvorný et al., 2010; Pokorný et al., 2014), which provides the mass, velocity and radiant distributions for these three solar system bodies, to model the injection rate profiles of a range meteoric metals into their respective atmospheres. In summary, we assess the absolute contribution of each cosmic dust source at Earth, and then extrapolate to Mars and Venus to determine the global mass influx accreted by these planets, together with the mass fraction that ablates or remains as spherules and unmelted micrometeorites. The Fe:Ni ratio in a planetary atmosphere provides a sensitive test of the new multiphase version of CABMOD. For Earth, this ratio is compared to lidar and sub-orbital rocket observations; and for Mars, measurements of metallic ions by the NGIMS instrument on MAVEN. Finally, there is a discussion about the deposition of meteoritic organic matter to the Martian soil, and its potential fate.

2. The zodiacal cloud model for Venus, Earth, and Mars

The Zodiacal Cloud model (ZoDy) is a dynamical model which describes the temporal and orbital evolution of sub-mm cosmic dust particles from their sources (Jupiter Family Comets, Asteroids, Halley Type Comets, and Oort Cloud Comets) to sinks (sublimation, impact on a solar system body or departure from the solar system) (Nesvorný et al., 2011; Nesvorný et al., 2010). In the ZoDy, each particle is tracked assuming the influence of planetary gravitational attraction, radiation pressure, and the Poynting-Robertson and solar wind drag. The model was originally constrained by observations of infrared emission from the Zodiacal Cloud, measured by the Infrared Astronomical Satellite (IRAS) (Reach, 1988; Reach, 1992; Reach et al., 1997), and more

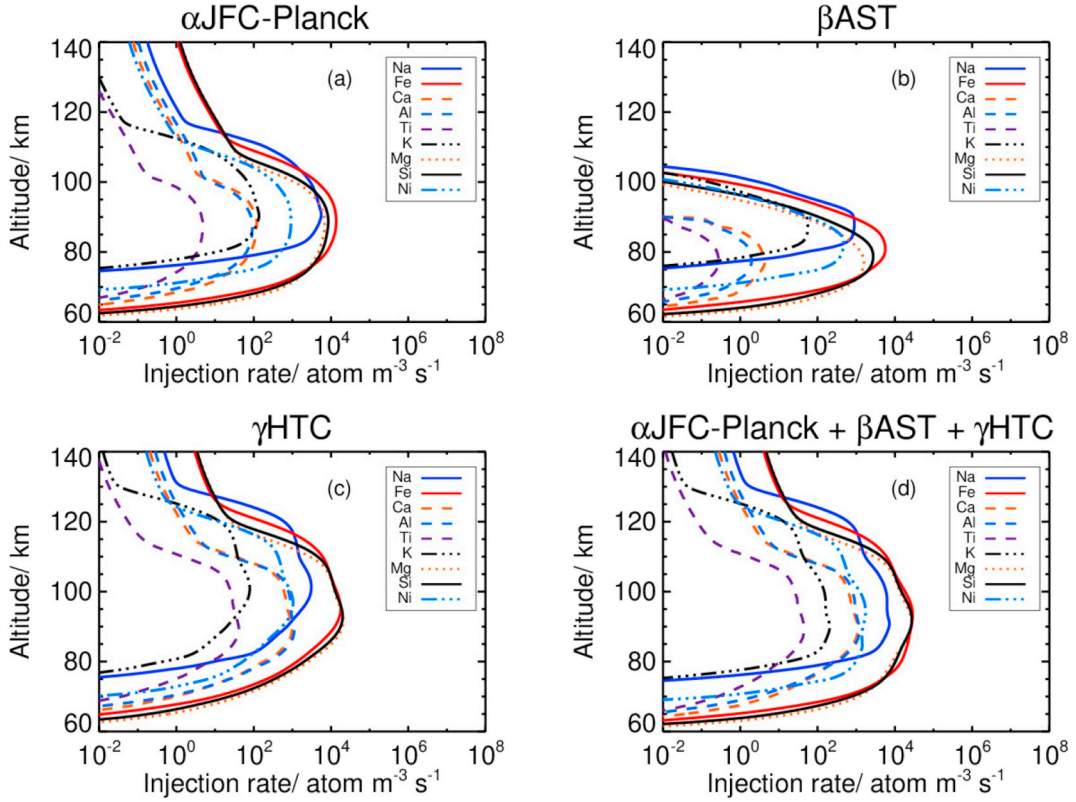

Fig. 3. (a), (b) and (c): Injection deposition profiles for the main metal constituents integrated over the JFC (constrained with the Planck observations), AST and HTC cosmic dust sources in Earth's atmosphere. (d): global ablation rates for Earth.

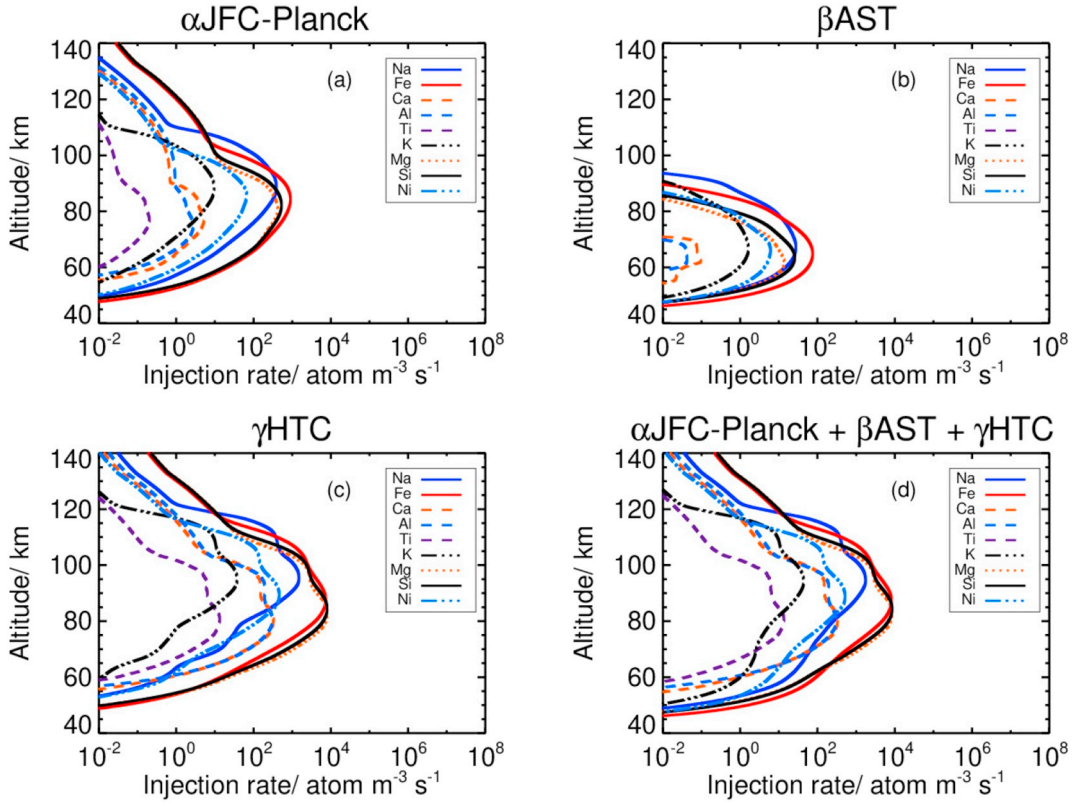

Fig. 4. (a), (b) and (c): Injection deposition profiles for main metal constituents integrated over the JFC (constrained with the Planck observations), AST and HTC cosmic dust sources in the Martian atmosphere. (d): global ablation rate for Mars.

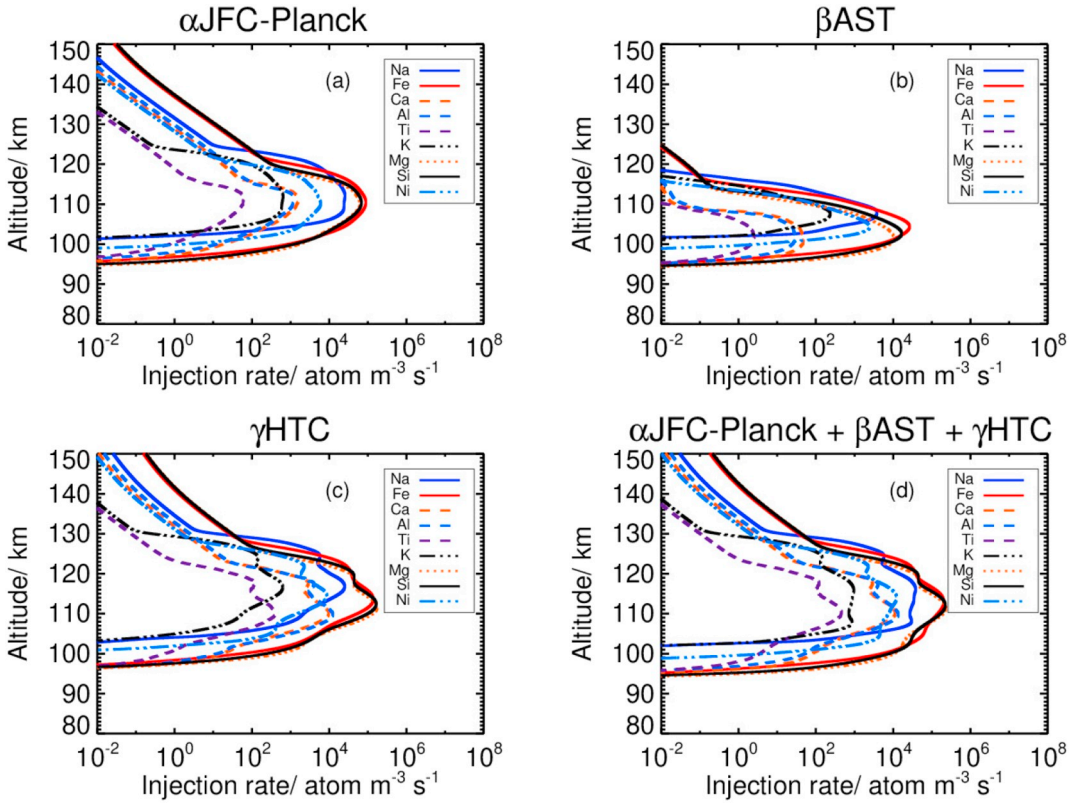

Fig. 5. (a), (b) and (c): Injection deposition profiles for main metal constituents integrated over the JFC (constrained with the Planck observations), AST, and HTC cosmic dust sources at Venus (night side). (d): global ablation rate for Venus on the night side.

recently, the Planck satellite which covers a greater spectral range (Ade et al., 2014). As discussed in Carrillo-Sánchez et al. (2016), the size distributions of cosmic dust constrained by the IRAS and the Planck observations are assumed to be represented by a broken power law defined by a break diameter D_{break}. The JFC-IRAS observations suggested that D_{break} ~100 μm (Nesvorný et al., 2011; Nesvorný et al., 2010), whereas the JFC-Planck observations indicate an average D_{break} ~36 μm (Fixsen and Dwek, 2002). Previously, we used an earlier version of CABMOD (Vondrak et al., 2008) combined with the ZoDy model to quantify the mass contribution of each cosmic dust source into the Earth's upper atmosphere (Carrillo-Sánchez et al., 2016). The original version of CABMOD assumed a single monolithic olivine phase and the vapour pressures were estimated directly from the MAGMA thermodynamic module (Fegley and Cameron, 1987; Schaefer and Fegley, 2004); this simplification does not reproduce satisfactorily the Fe evaporation profile observed in laboratory experiments using a Meteoric Ablation Simulator (MASI) (Bones et al., 2019; Gómez-Martín et al., 2017). This is largely because Fe-Ni metal alloy and FeS are commonly found in chondritic meteorites, especially in H-type ordinary chondrites (Jarosewich, 1990), and are thought to play an important role in the formation of the Earth and other planets resulting in core formation in rocky planets and asteroids.

The new version of CABMOD, termed CABMOD 3 (Bones et al., 2019), includes a multiphase treatment to account for both the silicate and FeNi metal phases in IDPs. The Fe partitioning between the silicate bulk and the Fe-Ni metal grains and FeS sulfide clumps in CABMOD 3 has been estimated from the chemical analysis provided by Jarosewich (1990) (see Table S1 in the Supporting Information). CI chondrites are a rare group where their original parent body has been extensively modified by aqueous alterations at ~323 K–423 K and subsequent thermal metamorphism (Endress et al., 1996; Zolensky et al., 1989), which leads to the absence of chondrules, CAI inclusions, and metal grains. In the case of CI chondrites, non-silicate Fe (hereafter Fe (m + S), where m and S refers to FeNi alloy grains and FeS inclusions, respectively) is mainly located in pyrrhotite ($[Fe,Ni]_{1-x}S$, with x between 0 and 0.125) and pentlandite ($[Fe,Ni]_9S_8$) inclusions (Bullock et al., 2005). Therefore, for the purposes of this study, FeS domains in CI chondrites are treated as unique containers of metallic Fe in CABMOD 3 (Bones et al., 2019). In fact, during the atmospheric entry, Fe-FeS domains start melting at 1261 K (Burgess et al., 1991; Greshake et al., 1998), thus low-Fe solids and liquids separate from solid Fe, leading to the evaporation of sulfur from these phases until only FeNi alloy grains are left (Walder and Pelton, 2005; Waldner and Pelton, 2004). Consequently, it may be inferred that most sulfur is deposited in the upper atmosphere and does not reach the surface (Gómez Martín et al., 2017).

Silicate and metal phases are completely immiscible (Hutchinson, 2004), and hence are treated independently in the model (Bones et al., 2019). As shown in Jarosewich (1990) (see Table S1 in the Supporting Information), about one-third of the total Fe content in CI chondrites is distributed in FeS grains, which gives an average Fe(m + S):Ni ratio of 5.51 for Ni-bearing metal domains, and in accordance with these estimates, ~70% of the total Fe is embedded inside the silicate bulk. To model the mass loss rate from metal grains, CABMOD 3 uses a thermodynamic module to estimate the vapour pressures for pure metallic Fe and Ni from the JANAF thermodynamic tables (Chase et al., 1985). These pressures are applicable to an ideal solution and subsequently need to be corrected by the corresponding Raoultian activity coefficients for a given particle composition and temperature (Conard et al., 1978). Both MAGMA and the Fe-Ni thermodynamic modules are called simultaneously by CABMOD when the respective melting point of each phase is reached. The phase diagram for a binary Fe-Ni system shows that for an average CI Fe(m + S):Ni ratio of 5.51, metal grains melt completely at 1760 K (Swartzendruber et al., 1991), near to the melting temperature of ~1800 K adopted in CABMOD for an olivine phase with a chondritic Fe:Mg ratio of 0.84 (Vondrak et al., 2008). Fig. S1 in the

Table 1
Global mass input from the three cosmic dust sources for Earth, using the JFC-Planck fit. Elemental ablation inputs are italicized; the percentages in parentheses show the fraction of each element that ablates from its total atmospheric input from each source. The table also shows the partition of ablated atoms between silicate and metal phases.

Mass flux		JFC (t d^{-1})	AST (t d^{-1})	HTC (t d^{-1})	Total (t d^{-1})
Unmelted micrometeorites		13.38	0.62	0.17	14.17
Cosmic spherules		3.73	1.34	0.38	5.45
Total ablated atoms		2.51	0.66	5.16	8.33
Ablated atoms from silicate		1.98	0.49	4.61	7.08
Ablated atoms from FeNi		0.53	0.17	0.55	1.25
Cosmic spherules[a]		2.83	1.31	0.33	4.47
Unmelted ($r > 50\ \mu m$)		5.83	0.61	0.11	6.55
Unmelted ($T \leq 900\ K$)		0.71	0.031	0.043	0.78
Unaltered Carbon		0.036	1.6×10^{-3}	2.1×10^{-3}	0.040
	Na	*0.14 (39%)*	*0.018 (91%)*	*0.11 (99%)*	*0.27 (54%)*
	K	*6.1×10^{-3} (37%)*	*2.0×10^{-3} (89%)*	*4.7×10^{-3} (99%)*	*0.013 (56%)*
	Fe	*1.1 (19%)*	*0.30 (40%)*	*1.5 (91%)*	*2.8 (36%)*
	Ni	*0.070 (22%)*	*0.025 (58%)*	*0.091 (96%)*	*0.18 (39%)*
	Si	*0.31 (10%)*	*0.081 (19%)*	*0.84 (90%)*	*1.2 (27%)*
	Mg	*0.21 (7%)*	*0.044 (11%)*	*0.73 (88%)*	*0.98 (24%)*
	Ca	*5.7×10^{-3} (2%)*	*2.0×10^{-4} (0.5%)*	*0.058 (73%)*	*0.064 (16%)*
	Al	*2.9×10^{-3} (1%)*	*6.0×10^{-5} (0.2%)*	*0.047 (64%)*	*0.050 (14%)*
	Ti	*2.8×10^{-4} (2%)*	*1.5×10^{-5} (0.8%)*	*2.9×10^{-3} (73%)*	*$3.2\ 10^{-3}$ (16%)*
	O	*0.69 (10%)*	*0.19 (20%)*	*1.8 (89%)*	*2.7 (27%)*
Total		**19.62**	**2.62**	**5.71**	**27.95**
Total silicate		**17.64**	**2.35**	**5.13**	**25.12**
Total FeNi		**1.98**	**0.27**	**0.58**	**2.83**

[a]Spherules in the size range $50\ \mu m \leq r \leq 700\ \mu m$ corresponding to measurements at South Pole (Taylor et al., 1998).

Supporting information shows Na, Fe, and Ni ablation profiles for two IDP analogues, comparing MASI experiments and CABMOD simulations.

2.1. Mass and velocity distributions of Cosmic Dust

Fig. 1 shows the mass and velocity distributions for JFC, AST and HTC accreted by the Earth, Mars and Venus, predicted by the ZoDy model and constrained by the Planck observations of infrared emission from the Zodiacal Cloud. These histograms are weighted following the fitting procedure discussed in more detail in Section 2.2. Carrillo-Sánchez et al. (2016) concluded that the mass contribution of JFCs for the Earth using the observations constrained by Planck and IRAS observations is 80% and 57%, respectively. These results show that JFCs are the main contributor to the terrestrial cosmic dust input. The Planck distribution is somewhat closer to the conclusions of several studies (Nesvorný et al., 2010; Rowan-Robinson and May, 2013; Yang and Ishiguro, 2015; Zook, 2001). Hence, all results in the present work are referred to the JFC-Planck particle mass distribution (see Section 2.2 for more details). Moreover, HTCs and OCCs are fast particles that essentially ablate completely, making it difficult to distinguish the relative contributions of these two sources to the global influx rate using the method of Carrillo-Sánchez et al. (2016). As such, HTCs will be considered here as the sole contributor for fast particles, that is, HTCs are assumed to represent all Long-Period cometary particles including OCCs.

The left-hand panels in Fig. 1 illustrate the histogram of the particle mass distribution for the three cosmic dust sources (JFC, AST, and HTC) and the three terrestrial planets in mass flux per decade over the mass range from 10^{-10} to 10^{-2} g. The radius range shown in the top abscissa varies between ~2 μm and ~1 mm, assuming a mass fraction for the silicate bulk of 90 wt% and a density of 2.2 g cm^{-3} (Consolmagno et al., 2008), while the mass fraction for metal Fe-Ni phase is 10 wt% with a density of 4.7 g cm^{-3} (Bones et al., 2019). The histograms show that JFC-Planck is the main contributor of small size particles, with a peak around ~0.01 μg, whereas the AST and HTC peaks are about ~10 μg, supplying the largest particles. The direct estimates of the global mass influx in the ZoDy for Earth, Mars, and Venus are 29.6 ± 14.8 t d^{-1}, 1.6 ± 0.8 t d^{-1}, and 31.5 ± 15.8 t d^{-1}, respectively. In the case of JFCs, the mass distributions predicted by the ZoDy model are constrained by Planck observations of the Zodiacal Cloud. However, the terrestrial mass inputs for the AST and HTC populations in the ZoDy model are arbitrarily set to 10 t d^{-1}, because their contributions to the global influx for each planetary atmosphere cannot be calibrated with sufficient accuracy from Zodiacal Cloud observations (Carrillo-Sánchez et al., 2016).

The right-hand panels in Fig. 1 show the mass influx as a function of the input speed derived directly from the ZoDy for the three planets. The entry speeds range between those for particles in prograde and retrograde orbits: 11.5–71.5 km s^{-1} for Earth, 5.5–59.5 km s^{-1} for Mars, and 10.5–85.5 km s^{-1} for Venus. In all cases, JFCs and ASTs represent the slowest populations with most of these particles originating

Table 2
Global mass input from the three cosmic dust sources for Mars, using the JFC-Planck fit. Elemental ablation inputs are italicized; the percentages in parentheses show the fraction of each element that ablates from its total atmospheric input from each source. The table also shows the partition of ablated atoms between silicate and metal phases.

Mass flux		JFC (t d^{-1})	AST (t d^{-1})	HTC (t d^{-1})	Total (t d^{-1})
Unmelted micrometeorites		0.93	0.26	0.038	1.23
Cosmic spherules		0.092	0.021	0.070	0.18
Ablated atoms		0.052	3.6×10^{-3}	0.59	0.65
Ablated atoms from silicate		0.040	2.4×10^{-3}	0.53	0.57
Ablated atoms from FeNi		0.012	1.3×10^{-3}	0.068	0.081
Unmelted ($T \leq 900\ K$)		0.26	0.013	7.0×10^{-4}	0.27
Unaltered Carbon		0.013	6.4×10^{-4}	3.5×10^{-5}	0.014
	Na	*3.8×10^{-3} (18%)*	*2.9×10^{-4} (14%)*	*0.013 (96%)*	*0.017 (47%)*
	K	*1.6×10^{-4} (18%)*	*3.0×10^{-5} (13%)*	*5.6×10^{-4} (95%)*	*7.5 10^{-4} (44%)*
	Fe	*0.022 (7%)*	*1.8×10^{-3} (2%)*	*0.18 (90%)*	*0.20 (34%)*
	Ni	*1.6×10^{-3} (9%)*	*1.5×10^{-4} (3%)*	*0.011 (92%)*	*0.013 (38%)*
	Si	*6.2×10^{-3} (3%)*	*2.7×10^{-4} (0.6%)*	*0.095 (83%)*	*0.10 (30%)*
	Mg	*4.2×10^{-3} (3%)*	*1.2×10^{-4} (0.3%)*	*0.082 (80%)*	*0.086 (29%)*
	Ca	*8.9×10^{-5} (0.6%)*	*1.0×10^{-6} (0.02%)*	*5.6×10^{-3} (56%)*	*5.7 10^{-3} (19%)*
	Al	*4.0×10^{-5} (0.3%)*	*2.9×10^{-7} (0.01%)*	*3.9×10^{-3} (42%)*	*3.9 10^{-3} (15%)*
	Ti	*4.3×10^{-6} (0.6%)*	*7.0×10^{-8} (0.03%)*	*2.7×10^{-4} (56%)*	*2.7 10^{-4} (19%)*
	O	*0.014 (4%)*	*9.3×10^{-4} (1%)*	*0.20 (82%)*	*0.21 (29%)*
Total		**1.08**	**0.28**	**0.70**	**2.06**
Total silicate		**0.97**	**0.25**	**0.63**	**1.85**
Total FeNi		**0.11**	**0.03**	**0.07**	**0.21**

mainly from Helion and anti-Helion radiants. In contrast, HTC particles which originate from apparent north and south sources are relatively fast, and therefore experience a higher degree of atmospheric ablation. The average input speeds for JFCs are 14.5 km s^{-1} (Earth), 11.0 km s^{-1} (Mars), and 15.2 km s^{-1} (Venus). In the case of AST particles, these values are 12.0 km s^{-1} (Earth), 6.5 km s^{-1} (Mars), and 11.4 km s^{-1} (Venus). The velocity distributions for HTC particles exhibit a dominant peak at 26.5 km s^{-1} (Earth), 21.5 km s^{-1} (Mars), and 29.5 km s^{-1} (Venus). Note that the average AST speed at Venus is lower than at Earth (in contrast to the JFC and HTC average speeds), because AST particles are in close-to-prograde orbits and so reflect the planetary escape velocity: 10.4 km s^{-1} for Venus and 11.2 km s^{-1} for Earth.

2.2. Modelling ablation and determining the contribution of each cosmic dust source

The integrated deposition profiles of the main meteoric metals in the atmospheres of Earth, Mars and Venus were then estimated by combining the ZoDy particle distributions with the new multiphase treatment implemented in CABMOD 3. The ZoDy model tracks the evolution of a large number of particles providing their masses, entry velocities, and radiants. In our previous study, Carrillo-Sánchez et al. (2016) used a Monte-Carlo method to sample the velocity and zenith angle distributions of each particle in the mass range between 10^{-3} and 10^{3} μg. For each of the three cosmic dust sources, each mass decade of the mass flux distribution was split into 5 mass bins. However, this mass sampling approach over-emphasises the contribution of the smaller bins within each mass decade to the total mass influx, leading to an overestimate of the flux of unmelted particles. For the present study we have changed the method of integrating over the mass distribution of each cosmic dust source, to be more consistent with the way in which the ZoDy model is formulated. The mass distribution in ZoDy is described by representative masses extending across the mass range. Each representative mass sits in a mass bin delimited by the geometric means of its mass with the representative masses on either side of it. This scheme, which is depicted in Fig. 2, shows the mass distributions of JFC-Planck, AST and HTC particles for Earth (note that the decadal mass fluxes of each cosmic dust source depicted in Fig. 1 are produced by interpolating the ZoDy mass distributions (Fig. 2) onto a decadal mass grid). Each representative mass bin is then populated with 500 particles of the representative mass, whose entry velocities and radiants are Monte Carlo selected. The particle size is determined assuming the particle is spherical and has a density of 2.2 g cm^{-3} (Consolmagno et al., 2008).

Each of the particles with representative mass, and selected entry velocity and radiant, is then run through CABMOD to determine its fate during atmospheric entry. For Earth, CABMOD is run assuming a constant atmospheric density profile for the conditions of March at 40°N

Table 3
Global mass input from the three cosmic dust sources for Venus (night side) using the JFC-Planck fit. Elemental ablation inputs are italicized; the percentages in parentheses show the fraction of each element that ablates from its total atmospheric input from each source. The table also shows the partition of ablated atoms between silicate and metal phases.

Mass flux		JFC (t d^{-1})	AST (t d^{-1})	HTC (t d^{-1})	Total (t d^{-1})
Unmelted micrometeorites		11.60	0.30	0.094	11.99
Cosmic spherules		5.19	0.99	0.22	6.40
Ablated atoms		4.26	0.66	7.67	12.59
Ablated atoms from silicate		3.48	0.51	6.86	10.85
Ablated atoms from FeNi		0.78	0.15	0.81	1.74
Unmelted ($T \leq 900\ K$)		0.29	0.016	0.036	0.34
Unaltered Carbon		0.014	8.1×10^{-4}	1.8×10^{-3}	0.017
	Na	*0.21 (53%)*	*0.014 (91%)*	*0.15 (99%)*	*0.37 (65%)*
	K	*9.1×10^{-3} (52%)*	*1.5×10^{-3} (91%)*	*6.6×10^{-3} (99%)*	*0.017 (66%)*
	Fe	*1.61 (27%)*	*0.29 (53%)*	*2.19 (97%)*	*4.09 (47%)*
	Ni	*0.11 (32%)*	*0.021 (67%)*	*0.13 (98%)*	*0.26 (51%)*
	Si	*0.58 (17%)*	*0.087 (27%)*	*1.23 (95%)*	*1.90 (38%)*
	Mg	*0.44 (14%)*	*0.052 (18%)*	*1.09 (94%)*	*1.58 (35%)*
	Ca	*0.016 (5%)*	*5.1×10^{-4} (2%)*	*0.096 (86%)*	*0.11 (25%)*
	Al	*8.3×10^{-3} (3%)*	*2.0×10^{-4} (0.8%)*	*0.083 (79%)*	*0.091 (23%)*
	Ti	*7.5×10^{-4} (5%)*	*3.0×10^{-5} (2%)*	*4.7×10^{-3} (86%)*	*5.5 10^{-3} (26%)*
	O	*1.27 (17%)*	*0.19 (28%)*	*2.69 (95%)*	*4.15 (38%)*
Total		**21.05**	**1.95**	**7.98**	**30.98**
Total silicate		**18.92**	**1.75**	**7.17**	**27.84**
Total FeNi		**2.13**	**0.20**	**0.81**	**3.14**

(https://omniweb.gsfc.nasa.gov/vitmo/msis_vitmo.html) (Hedin, 1991). For Mars, CABMOD uses the Mars Climate Database in winter at 40°N (http://www-mars.lmd.jussieu.fr/mcd_python/) (Lewis et al., 1999). Keating et al. (1985) reported the chemical and physical structure of Venus' atmosphere at different latitudes based on measurements from various spacecraft such as Venera 11 and 12 for the noon and midnight hemispheres, where there are significant differences because of the slow rotational period (116 Earth days). The results for the night side of Venus at the equator are presented here, given that CABMOD-ZoDy simulations do not show a significant variation in the dayside.

The panels in Figs. 3, 4, and 5 depict the integrated injection rates of individual elements as a function of height for Earth, Mars and Venus, respectively. Each figure shows the absolute injection rate profiles from each of the three cosmic dust sources, determined using the procedure discussed below (Carrillo-Sánchez et al., 2016), as well as the total input. In all cases, the alkali elements (Na and K) ablate about 10 km higher than the main compounds (Fe, Mg, and Si) and about 15 km higher than the more refractory metals (Ca, Al, and Ti). Note that Ni exhibits an ablation peak similar to Fe for all sources, which is expected given their similar volatility (Chase et al., 1985). As expected from their relative velocity distributions, the HTC particles ablate roughly 10 km and 20 km higher than JFCs and ASTs, respectively, as expected from their relative velocity distributions. For comparison, ablation occurs between 130 and 60 km at Earth, 120 and 40 km at Mars, and 130 and 95 km at Venus. The injection rate profiles for Earth peak ~10 km higher than for Mars, and ~20 km lower than for Venus.

Carrillo-Sánchez et al. (2016) determined the mass contribution of each cosmic dust source by fitting to three measured accretion rates. First, the global input of neutral Na at Earth is estimated to be 0.3 ± 0.1 t d^{-1}, using lidar measurements at the Starfire Optical Range (35°N) (Gardner et al., 2014). Second, the global input flux of neutral Fe is estimated to be 2.3 ± 1.1 t d^{-1} from lidar measurements at Table Mountain (40°N). Note that these measurements of Na and Fe are extrapolated globally from night-time measurements made at specific locations. Third, the global flux of spherules with diameters between 50 and 700 μm is estimated to be 4.4 ± 0.8 t d^{-1} from measurements in the South Pole water well (Taylor et al., 1998). The global mass accretion rate of Na atoms, Fe atoms or cosmic spherules can be written as:

$$\Psi_{total} = \alpha\Psi_{JFC} + \beta\Psi_{AST} + \gamma\Psi_{HTC} \quad (1)$$

where ψ_{JFC}, ψ_{AST} and ψ_{HTC} are the global mass accretion rates of Na, Fe or spherules from the different sources; and α, β and γ are the coefficients which weight the contribution from each source. A Monte Carlo model calculates the optimal contribution for the fluxes of Na, Fe, and spherules, assuming that cometary particles are enriched in Na by a factor of 2.5 (Carrillo-Sánchez et al., 2016). The optimized coefficients are $\alpha = 0.67 \pm 0.26$, $\beta = (2.48 \pm 1.78) \times 10^{-2}$, and $\gamma = (5.97 \pm 2.26) \times 10^{-2}$, which translate into global mass accretion rates at Earth for JFC, AST and HTC particles of 19.6 ± 7.5 t d^{-1} (70.2%), 2.6 ± 1.9 t d^{-1} (9.3%), and 5.7 ± 2.2 t d^{-1} (20.4%), respectively. Note that the current estimate of the total influx for Earth, 27.9 ± 8.1 t d^{-1}, is lower but within the uncertainty of our previous estimate (Carrillo-Sánchez et al., 2016). This decrease arises because the new integration method (see above) reduces the total unmelted mass flux by a factor of ~2. The HTC population to the total input mass is 10%

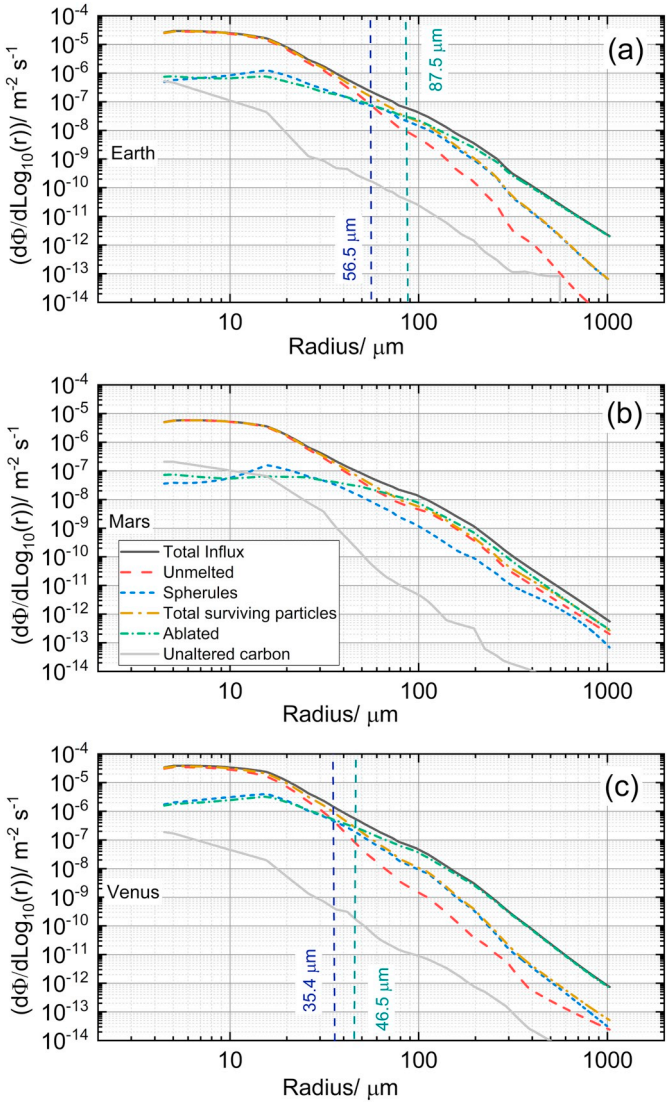

Fig. 6. Differential fluxes of particles for (a) Earth, (b) Mars, and (c) Venus. Black, red dashed, blue dashed, and yellow dot-dashed curves correspond to the total flux, and fluxes of unmelted particles, spherules, and total surviving particles, respectively. The green dot-dashed curve is the flux of particles which ablate. Grey curves show the fluxes of intact carbon. The vertical dashed blue lines in (a) and (c) represent the threshold particle size at which the spherule flux is larger than the flux of unmelted particles. The vertical dashed green line is the threshold size at which the ablation flux is larger than the flux of micrometeorites (i.e. spherules and unmelted particles). (For interpretation of the references to color in this figure legend, the reader is referred to the web version of this article.)

higher, and the JFC-Planck is lower by approximately 10%, with respect to our previous estimate (Carrillo-Sánchez et al., 2016). The large contribution from the JFC source is consistent with observations of the Zodiacal Cloud (Nesvorný et al., 2010; Rowan-Robinson and May, 2013; Yang and Ishiguro, 2015; Zook, 2001).

The statistical error to the terrestrial input, determined from the Monte Carlo fitting procedure to take account of uncertainties in the Na, Fe and cosmic spherule fluxes, is ± 29%. However, this does not include a number of other significant uncertainties e.g. in the extrapolation from the single point measurements of the lidar measurements to global Na and Fe fluxes, and uncertainties in the CABMOD model. Since these uncertainties cannot be properly quantified at the present time, we have – arbitrarily – doubled the uncertainty in the global dust input rate to ± 58%.

3. Discussion

3.1. Ablated mass and micrometeorite production

The coefficients α, β, and γ determined at Earth can now be used to scale the AST and HTC sources to the JFC source within the ZoDy model, and thus provide absolute dust inputs from all three sources to Mars and Venus. In the same way as for Earth (Section 2.2), Monte Carlo sampling across the velocity and entry angle distributions of each dust source can then be used to determine the fate of these particles on atmospheric entry. Tables 1, 2, and 3 list the partitioning of the total mass influx at the atmospheres of Earth, Mars, and Venus between unmelted particles, spherules, and ablated atoms for each of the three dust sources; the last column shows the total input. JFCs are the major contributor to the total accreted mass, with 70% for Earth, 68% for Venus and 52% for Mars, consistent with previous estimates (Nesvorný et al., 2010; Rowan-Robinson and May, 2013; Yang and Ishiguro, 2015; Zook, 2001). Note that the contribution of AST particles increases with the heliocentric distance with only 6% at Venus, 9% at Earth, and 14% at Mars, even though HTCs exhibit a larger impact in Mars – 34%, compared with 20% and 26% for Earth and Venus, respectively. According to the ZoDy model, JFCs experience a stronger gravitational focusing than HTCs at Earth and Venus, being markedly lower at Mars. Likewise, the collisional lifetime time of dust particles results in particles crossing Venus' orbit having experienced more collisions than those crossing the orbits of Earth and Mars. Accordingly these particles are dynamically more evolved and, therefore, a high fraction is completely destroyed by mutual collisions between meteoroids (Grün et al., 1985), leading to a lower contribution of the AST population at Venus orbit.

Table 2 shows that the global mass flux in the Martian atmosphere is estimated to be 2.1 ± 1.2 t d^{-1}, within the 0.086–8.6 t d^{-1} mass range determined by the LPW instrument on MAVEN (Andersson et al., 2015). Note that this range is derived from the sampling of small grains of radii from 1 μm to 12 μm; for comparison, CABMOD-ZoDy predicts a total input of 0.15 t d^{-1} in the radius range 4 μm - 12 μm. The total CABMOD mass flux of 2.1 ± 1.2 t d^{-1} is 7% of the terrestrial global input of 27.9 ± 16.2 t d^{-1}, and is significantly lower than previous estimates of the Martian mass flux, of around 50% of the terrestrial flux (Adolfsson et al., 1996; Borin et al., 2017). This discrepancy is mainly produced by two factors: first, the ZoDy model is constrained by the measured orbital distribution of meteors (Nesvorný et al., 2010; Nesvorný et al., 2006), which restricts the contribution of the AST meteoroids to the total cosmic dust density in the Zodiacal Cloud, whereas Borin et al. (2017) calibrated the flux at Earth by using an updated assessment of the Long Duration Exposure Facility (LDEF); second, as stated above, the ZoDy model considers that long-time evolved particles may be completely destroyed before crossing a planet's orbit, whilst Borin et al. (2017) computed the evolution of the particles' trajectories without collisional lifetime limits. Borin et al. (2017) also estimated a dust flux on Venus of 18.9 ± 1.5 t d^{-1}, a factor of 1.6 lower than our estimate of 31.0 ± 17.7 t d^{-1}.

Mars and Venus represent opposite extremes of the dust velocity distributions (Fig. 1), which results in a higher ablation efficiency of 41% in Venus' atmosphere. Nonetheless, Earth and Mars exhibit similar ablation yields of~ 30%, due to the larger contribution of HTCs at Mars. In all three cases, < 20% of the ablated atoms arise from Fe-Ni metal grains. Tables 1, 2, and 3 show that most of the incoming mass survives as unmelted particles with a mass fraction ranging from 39% in Venus to 60% in Mars, mostly originating from JFCs (Fig. 1a, c, and e illustrate the distribution of unmelted particles as a function of size). The differential fluxes of particles as a function of particle radius (4–1000 μm) for Earth, Mars, and Venus are plotted in Fig. 6. Note that the threshold particle size for which ablation exceeds survival is ~87.5 μm for Earth, compared with only ~46.5 μm for Venus because of the higher average entry velocity at Venus, which causes smaller dust particles to ablate.

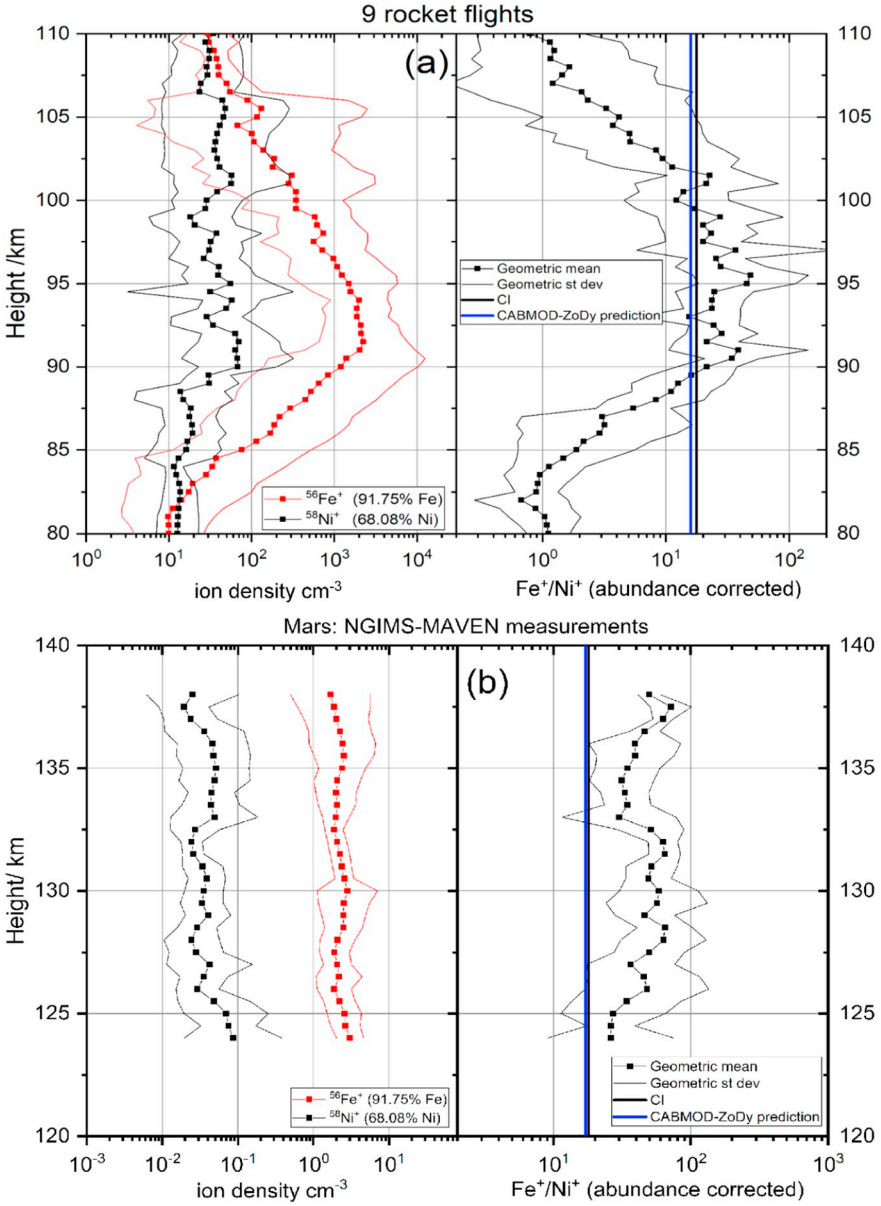

Fig. 7. Geometric mean densities of $^{56}Fe^+$ and $^{58}Ni^+$ and Fe^+/Ni^+ ratios versus height for (a) Earth, measured by 9 rocket flights and (b) Mars, measured by the NGIMS instrument on MAVEN. The abundance ratios are corrected for isotopic abundances of the metals, and the blue vertical lines indicate the CABMOD-ZoDy prediction. The Fe:Ni ratio at Earth is 20^{+13}_{-8} between 85 and 100 km, close to the chondritic ratio and the CABMOD-ZoDy prediction of 16 (right-hand panel in (a)), whereas the average measured Fe:Ni ratio at Mars is 43^{+13}_{-10}, a factor of 2.5 higher than the CABMOD-ZoDy prediction (right-hand panel in (b)). (For interpretation of the references to color in this figure legend, the reader is referred to the web version of this article.)

In contrast, the flux of micrometeorites surviving atmospheric entry at Mars is comparable in magnitude to the relative rate of ablation above 70.9 μm, given that most of the dust particles entering Mars' atmosphere do not melt. This is a much higher fraction than survive in Earth's and Venus' atmosphere. Flynn and McKay (1990) and Flynn (1991) inferred a total dust flux at Mars of 33 t d^{-1} from estimates of the mass influx at Earth (Hughes, 1978) and predictions of the Mars/Earth flux ratio derived from crater impacts in the Martian surface along with the dynamical evolution of particles close to Mars' orbit. Flynn (1996) reported an unmelted mass fraction of 72% at Mars. Although in the present study we estimate a total flux that is an order of magnitude smaller, the unmelted mass fraction is clearly dominant at 60% (Table 2), and these particles provide a potentially important source of organic matter to the Martian surface (Flynn, 1996), as discussed in Section 3.3.

Ablated metal atoms (including Si) undergo oxidation with O_3, O_2, CO_2, and H_2O to form oxides, hydroxides, carbonates and silicates, which polymerize into meteoric smoke particles (MSPs) (Plane et al., 2015). In the Martian mesosphere, metal carbonates should form H_2O clusters that can act as nuclei for the formation of CO_2-ice clouds (Plane et al., 2018). This is analogous to MSPs nucleating H_2O-ice (noctilucent) clouds in the terrestrial mesosphere (Duft et al., 2018). Frankland et al. (2017) demonstrated that Fe-rich MSPs provide a suitable surface for high-temperature heterogeneous chemistry in the lower atmosphere of Venus below 40 km, causing oxidation of CO to CO_2 and depletion of O_2.

3.2. Determining the elemental metal production: constraints on the nickel influx

Tables 1, 2, and 3 also list the individual ablation efficiencies of a range of metals in the atmospheres of the three planets. In the case of a

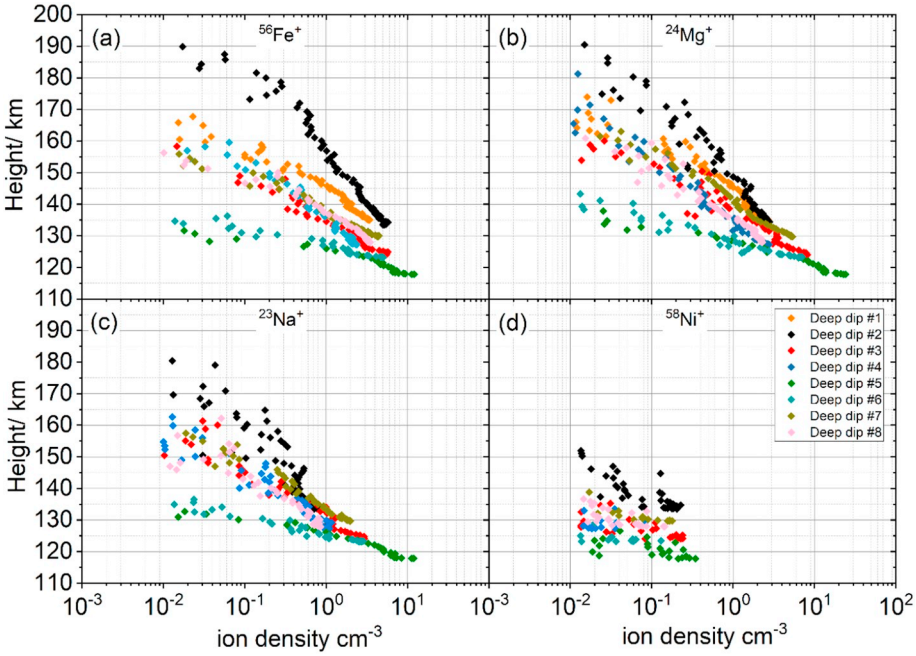

Fig. 8. Vertical density profiles for $^{56}Fe^+$, $^{24}Mg^+$, $^{23}Na^+$, and $^{58}Ni^+$ measured by the NGIMS instrument on MAVEN during eight deep dip campaigns.

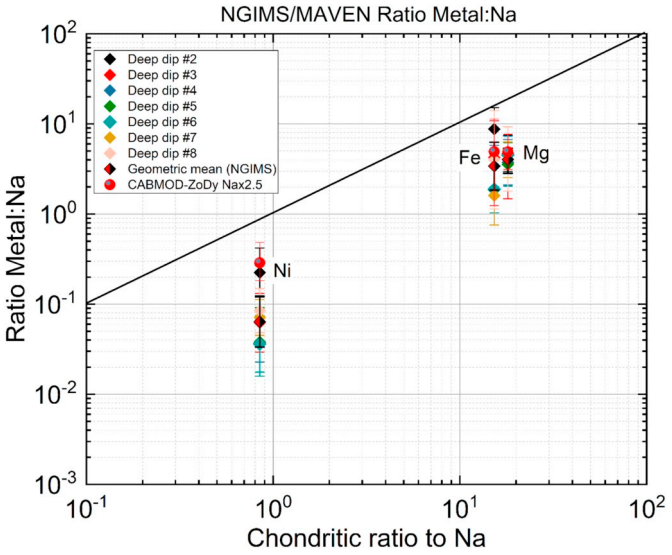

Fig. 9. Ratios of Fe, Mg, and Ni relative to Na for several deep dip campaigns, measured by the NGIMS instrument on MAVEN. The ratios are the geometric mean of each vertical profile. The red circles are the ratios predicted by CABMOD-ZoDy for Mars. (For interpretation of the references to color in this figure legend, the reader is referred to the web version of this article.)

relatively volatile element such as Na, the ablation efficiencies from JFC particles are 39% (Earth), 18% (Mars), and 53% (Venus). In contrast, for HTCs these efficiencies are much higher: 99% (Earth), 96% (Mars), and 99% (Venus). Note that JFCs are the main contributor to the Na ablation rates at Earth (52%) and Venus (57%), but not at Mars (22%). In contrast, for a highly refractory element such as Ca, the contribution from HTCs dominates: 91% (Earth), 98% (Mars), and 87% (Venus). For Mars, HTCs are the main contributor to the ablation fluxes of all metals.

In this Section we compare atmospheric measurements of metal ions and neutral atoms with CABMOD predictions. Following the discussion in the Introduction about fast neutral-ion cycling, we assume here that the ratios of metal ions or neutral atoms map closely onto their relative ablation fluxes (i.e. differences in the rate coefficients of analogous reactions have a secondary effect). The focus in this Section will be on Ni, since this is a key indicator of the multi-phase treatment in CABMOD 3. The percentage of Ni that ablates is 39% (Earth), 38% (Mars), and 51% (Venus), similar to the percentage yields of Fe. The global Ni ablation rate is 0.18 t d^{-1} (Earth), 0.013 t d^{-1} (Mars), and 0.26 t d^{-1} (Venus). Yen et al. (2006) analyzed Martian soil samples using Ni as a tracer to assess the meteoritic contributions to the surface materials and, according to the APXS data from the Mars Exploration Rovers, the measurements are consistent with a 1% to 3% chondritic input. The CI chondritic Fe:Ni ratio is 18.0 (Lodders and Fegley, 2011), which is in good agreement with the average chemical abundances derived from the mass spectroscopic analysis of Halley's cometary dust grains of VEGA-1 (Jessberger et al., 1988), and the study of nm-size grains by the Stardust mission to Jupiter-Family comet 81P/Wild 2 (Rietmeijer, 2009). Most recently, Stenzel et al. (2017) reported that the Fe:Ni ratio of particles retrieved from the coma of comet 67P/Churyumov-Gerasimenko is similar to the Allende (CV3), Murchinson (CM2) and Lancé (CO3.5) meteorites, and CI chondrites (Bones et al., 2019; Clarke et al., 1971).

Ni^+ ions have been measured in the Earth's ionosphere by rocket-borne mass spectrometry. Kopp (1997) determined a mean Fe:Ni ratio of 25.1, a factor of 3 larger than the ratio of $7.7^{+3.2}_{-10}$ measured in stratospheric sulfate particles (Cziczo et al., 2001). Fig. 7a shows the average Fe:Ni ratio for 9 rocket flights (Cziczo et al. (2001); Kopp E., University of Bern, per. comm.), where we include a correction for the isotopic abundances of $^{56}Fe^+$ and $^{58}Ni^+$. This yields a Fe:Ni ratio of $20.0^{+13.0}_{-8}$ between 85 and 100 km which is close to the CI ratio and is in good agreement with the CABMOD prediction of 15.9 (Table 1). Collins and M. (2015) reported the first observations of the mesospheric Ni atom layer, using a resonance lidar at Chatanika, Alaska (65°N, 147°W). The layer peaks at 87 km, with an Fe:Ni ratio of ~1.2. Given the similar volatility of Fe and Ni (Table 1), these observations would indicate that IDPs are enriched in Ni relative to Fe by a factor of ~15 compared with CI chondrites, which clearly contradicts the analysis of fresh cometary dust (see above), and the Fe:Ni ratio measured on IDPs that survived atmospheric entry (Arndt et al., 1996). However, more recent lidar observations by Gerding et al. (2018) at Kühlungsborn, Germany (54°N, 12°E) during late winter report a Fe:Ni ratio of 38 ± 11 (the uncertainty is estimated from the range in the Ni measurements and the

harmonic fit uncertainty for the mid-latitude Fe layer from Kane and Gardner (1993)). This is a factor of 2.4 ± 0.7 times higher than the ablation ratio predicted by CABMOD-ZoDy, which is probably explained by Ni being converted more efficiently than Fe to long-term sinks in the upper mesosphere.

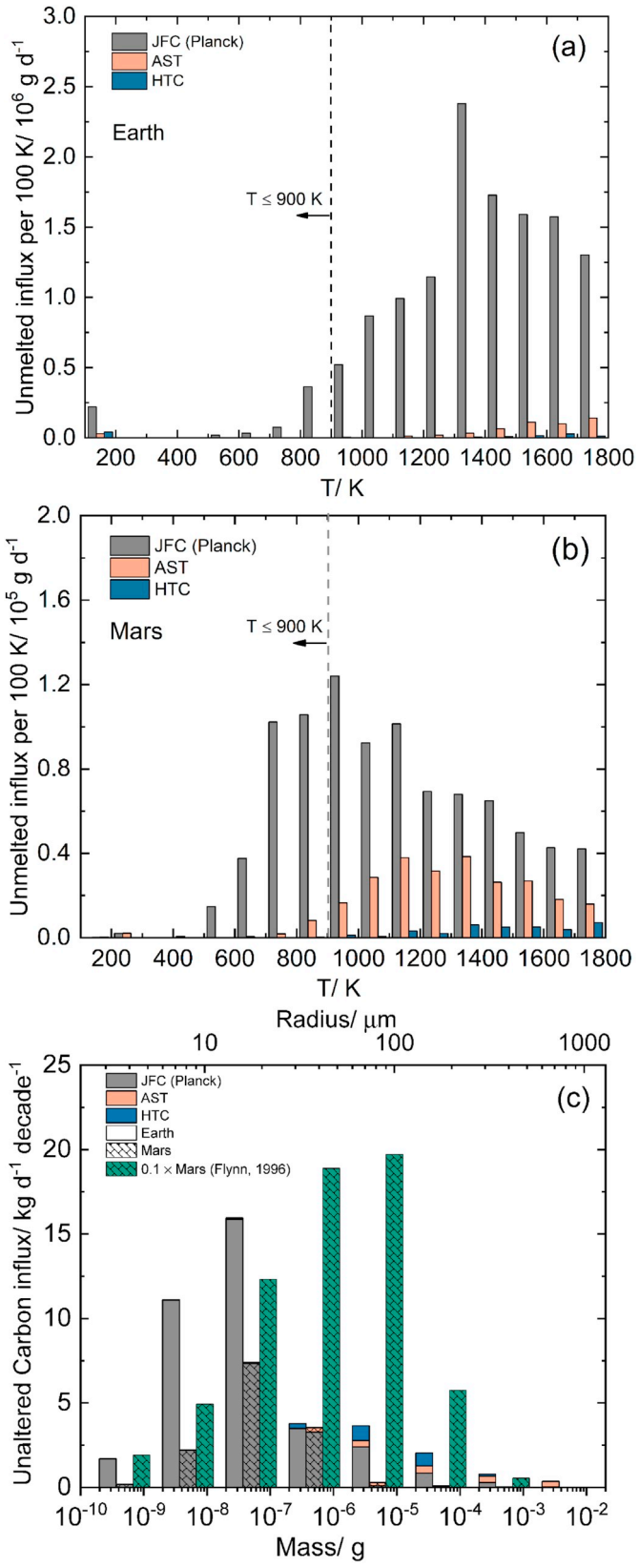

Fig. 10. Histograms illustrating the mass flux of unmelted particles over a range of temperatures below the melting point of the silicate phase (~1800 K) into the atmospheres of (a) Earth, and (b) Mars, for three cosmic dust sources (JFC in grey, AST in orange, and HTC in blue). The vertical dashed line shows the pyrolysis temperature of carbon (~900 K) (Anders, 1989) below which carbon remains intact; (c) histograms of the unaltered carbon influx for Earth and Mars (shaded bars) predicted by CABMOD-ZoDy and partitioned for the three cosmic dust sources. The histogram also displays the flux of carbon reported by Flynn et al. (1996) (green, shaded), scaled down by a factor of 0.1 for a clearer comparison. Flynn et al. (1996) estimated that the largest mass contribution of unaltered carbon occurs with a particle radius between 48 and 103 μm, whereas CABMOD-ZoDy predicts most of the contribution is from particles smaller than 20 μm. (For interpretation of the references to color in this figure legend, the reader is referred to the web version of this article.)

In the case of Mars, the NGIMS instrument onboard MAVEN (Mahaffy et al., 2015a; Mahaffy et al., 2015b) measures both ionized and neutral species in the altitude range 120–500 km (Benna et al., 2015a; Benna et al., 2015b; Mahaffy et al., 2015a). Following the close encounter of Comet Siding Spring (C/2013 A1) with Mars on 19 October 2014 (Benna et al., 2015b), the metal average ratios, corrected for the isotopic abundances of all metals, at an altitude around 185 km are: Fe:Na = 1.54 ± 0.04, Mg:Na = 1.07 ± 0.03, Ca:Na = (9.3 ± 6.0) × 10^{-3} and Ni:Na = 0.086 ± 0.005. This suggests a significant enrichment in Na with respect to CI chondrites. Indeed, numerical modelling of Siding Spring dust particles, using CABMOD 3 with an entry velocity of 56 km s^{-1} and a dust size distribution from Moorhead et al. (2014), produces an optimized fit with a Na enrichment of 10, yielding Fe:Na = 1.5, Mg:Na = 1.8, Ca:Na = 0.1 and Ni:Na = 0.09. The modelled Fe:Ni ratio of 18.0 is also in very good agreement with the measured ratio of 17.8 ± 1.0.

More recently, MAVEN has carried out a number of lower altitude excursions into the Martian atmosphere. These "deep dip" orbits reached down to ~120 km (Table S2 in the Supporting Information shows the specific conditions for each deep dip campaign). Fig. 8 illustrates the vertical profiles of $^{56}Fe^+$, $^{24}Mg^+$, $^{23}Na^+$, and $^{58}Ni^+$ during eight deep dip campaigns. As reported by Grebowsky et al. (2017), all metal ions exhibit similar scale heights above the homopause despite the significant difference in atomic mass (between the lighter $^{23}Na^+$ and $^{24}Mg^+$, and the heavier $^{56}Fe^+$ and $^{58}Ni^+$). Fig. 9 shows the metal ion ratio relative to Na from each deep dip, plotted against the ablation ratio predicted by CABMOD-ZoDy (with Na enriched over CI by a factor of 2.5 (Carrillo-Sánchez et al., 2016)). Correcting for isotopic populations where appropriate, the average ratios from these campaigns are Fe:Na = $3.4^{+2.8}_{-1.6}$ and Mg:Na = $4.0^{+1.3}_{-1.2}$, in agreement with the CABMOD-ZoDy estimates of Fe:Na = 4.9 and Mg:Na = 4.9. In contrast, the average Fe:Ni ratio measured by NGIMS (see Fig. 7b) is $42.6^{+13.4}_{-10.2}$, whereas the CABMOD-ZoDy prediction is 17.1, a factor of 2. $5^{+0.8}_{-0.6}$ times lower, similar to the lidar observations at Earth (Gerding et al., 2018). Again, the implication is that the Ni is converted into permanent reservoirs more efficiently than Fe at heights below 100 km, around the ablation maximum (Fig. 3).

3.3. Organic matter in the Martian atmosphere

Organic matter in carbonaceous chondrites occurs in different forms (Sephton and Botta, 2008): free organic matter such as amino acids, alkanes, alkylbenzenes, or carboxylic acids; refractory organic matter which may degrade with O_2 at high temperatures; and polymeric organic material such as kerogen (Hayatsu et al., 1977; Hayatsu et al., 1980), that may contribute up to 70% of the total organic matter in CI1 meteorites. There is also a small fraction of inorganic carbonates, mainly $MgCO_3$ and $FeCO_3$, that are commonly identified in Martian meteorites (McKay et al., 1996; Sephton et al., 2002), as well as at the surface of Mars (Orofino et al., 2000; Palomba et al., 2009). The

abundance of indigenous carbon in carbonaceous chondrites is between 2 and 5 wt%. For example, Fredriksson and Kerridge (1988) reported a total carbon content in CI1 Orgueil samples of 2.80 wt%. It has been proposed that IDPs are the main contributor of organic molecules to planetary surfaces by two orders-of-magnitude over other sources such as cometary and asteroidal impacts (Chyba and Sagan, 1992).

Anders (1989) determined an average pyrolysis temperature for organic compounds in meteorites of ~900 K. Fig. 10a and b show the mass influx of unmelted particles per 100 K temperature interval as a function of maximum temperature reached, for Earth and Mars, respectively. The contributions from the JFC, AST and HTC sources are shown, up to the silicate melting temperature of 1800 K. Fig. 10c shows the mass input per mass decade of particles which do not reach the carbon pyrolysis temperature, and hence may supply carbon to the surface of Mars and Earth (following the same procedure used by Flynn (1996)). CABMOD-ZoDy predicts a mass influx of particles not heated above ~900 K of 0.78 t d^{-1} for Earth, three times larger than at Mars with 0.27 t d^{-1}. Nonetheless, this result is somewhat different in terms of the fraction of unmelted mass that never reaches the pyrolysis temperature, with 22% at Mars and only 5% at Earth. Thus, a substantial fraction of the input particles do not experience severe heating in the Mars' atmosphere because of the lower atmospheric entry velocity, as shown in Fig. 10. Therefore, assuming that all carbon present in chondrites is of organic origin and a total C content of 5 wt% (Lodders and Fegley, 2011), the accretion rate of exogenous intact carbon is 0.040 t d^{-1} at Earth and 0.014 t d^{-1} at Mars. Fig. 10 shows that small particles (radius $<$ 20 μm) dominate amongst those that are not heated above 900 K, allowing preservation of organics. This is consistent with the scarcity of ultra-carbonaceous micrometeorites in the larger particles (20–30 μm) in Antarctic collections (Noguchi et al., 2015). Flynn (1996) estimated a flux of unaltered carbon at Mars of 0.66 t d^{-1}, by considering a total C content of 10 wt% with the largest mass contribution from particles with radii between 48 and 103 μm. In contrast, CABMOD-ZoDy predicts that 97% of the unaltered carbon-bearing particles at Mars are smaller than 48 μm radius (Fig. 10c). Note that if the Flynn (1996) model assumed a 5 wt% of intact carbon, then the fraction of intact C relative to the total unmelted influx would be ~1%, similar to CABMOD-ZoDy.

An important question is the fate of the organic molecules that reach the surface of Mars. The results from the Viking missions in 1976 are somewhat contradictory: on the one hand, CO_2 release was detected via aqueous oxidation from samples of Martian soil (Levin and Straat, 1979a; Levin and Straat, 1979b); on the other hand, GC–MS experiments did not evidence any organic volatile molecules from heated samples, as well as no by-product from pyrolysis of organic matter (Biemann et al., 1976). Benner et al. (2000) suggested that the Martian regolith is likely to be oxidizing due to UV radiation photolysing of H_2O, and subsequent OH and H radical chemistry producing peroxides and other oxidizing compounds. Additionally, sulfate minerals present in the Martian regolith, such as iron sulfate, can decompose over a broad range of temperatures, releasing oxygen that may potentially oxidize organic molecules (Lewis et al., 2015). Benner et al. (2000) proposed that organic molecules are mainly converted to carboxylic acids under oxidizing conditions with a production yield of benzenecarboxylic acid of 10%. Therefore, they estimated that roughly 2 kg m^{-2} of benzenecarboxylic acid has been produced in the Martian soil during the last 3 Gyr, which means an average concentration of ~500 ppm in the first meter of surface. According to CABMOD-ZoDy, the total amount of intact carbon deposited is 0.04 kg m^{-2} with an average concentration of ~10 ppm in the top meter. This would be challenging to measure, given that the detection probability of current techniques such as Pyrolysis Fourier Transform Infrared Spectroscopy is ~17% in the 4–21 ppm range, and ~56% in the 22–43 ppm range (Gordon and Sephton, 2016). More recently, the Sample Analysis at Mars (SAM) instrument onboard Rover Curiosity was able to confirm for the first time the presence of some unoxidized organic molecules – including thiophenic and aromatic compounds - in the Martian soil (Loes ten Kate, 2018).

Finally, one should note that many meteoroids fragment during atmospheric entry (Subasinghe et al., 2016), which is most likely caused by the thermal failure of the interstitial cement binding together the grains within a meteoroid. The cement is likely to have an organic component (Flynn et al., 2003), and fragmentation would cause the loss of some organic fraction of the original dust particle during entry. However, the resulting fragments - being significantly smaller - are much less likely to reach the pyrolysis temperature (Brooke et al., 2017). Hence, fragmentation may actually lead to an increased amount of organics reaching the surface.

4. Summary and conclusions

In this study a new multiphase treatment has been implemented in the chemical ablation model CABMOD to account for both the olivine bulk and metallic grains in cosmic dust particles. The contribution of three cosmic dust sources – JFCs, ASTs and HTCs - into the Earth's atmosphere, predicted by the Zodiacal Dust Model (ZoDy), was then reassessed and extrapolated to Mars and Venus. JFCs contribute the most mass to all three planetary atmospheres, with 70% for Earth, 52% for Mars, and 68% for Venus. This amounts to a total mass input of 27.9 ± 8.1 t d^{-1} for Earth, 2.1 ± 1.0 t d^{-1} for Mars, and 31.0 ± 15.5 t d^{-1} for Venus, respectively. The relative mass contribution of AST particles increases with the heliocentric distance, being 6% for Venus, 9% for Earth, and 14% for Mars.

The threshold particle radius for which the ablated mass is larger than the mass surviving entry is 87.5 μm for Earth, and 46.5 μm for Venus, with overall ablation efficiencies of 30% and 41%, respectively. In contrast, the accretion rate of unmelted particles at Mars is 60% of the overall influx mass, providing a fluence of intact carbon (contained in particles that do not reach the pyrolysis temperature of 900 K) of 0.014 t d^{-1}. The resulting concentration of organics in the top 1 m would then be around 10 ppm, making it challenging to detect. Lastly, the CABMOD-Zody predictions of the ratio of Fe^+ to Ni^+ ions in the terrestrial atmosphere are in good agreement with available measurements from sub-orbital rockets, and also with measurements made in the Martian ionosphere immediately following the passage of Comet Siding Spring. However, lidar observations of Ni and Fe at Earth, and MAVEN-NGIMS measurements of the ions during deep dip orbits into the Martian atmosphere, indicate that Ni is depleted with respect to Fe by a factor of ~2.5 with respect to CABMOD-ZoDy estimates. This suggests that Ni is converted to permanent reservoirs more efficiently than Fe.

Acknowledgements

This work is supported by the UK Natural Environment Research Council (grant number NE/P001815/1). J.C.G.-M. acknowledges funding from the Spanish Ministry of Science through the Instituto de Astrofísica de Andalucía-CSIC, Centro de Excelencia Severo Ochoa under grant SEV-2017-0709. D.N. is supported by NASA's Solar System Exploration Research Virtual Institute (SSERVI). P.P. is supported through the NASA's Solar System Workings (SSW). M.B. is supported through the NASA Mars Exploration Program. G.J.F. is supported by NASA Emerging Worlds grant NNX19AE59G. The MASI data and CABMOD output are archived at the Leeds University PETAL (PetaByte Environmental Tape Archive and Library; http://www.see.leeds.ac.uk/business-and-consultation/facilities/petabyte-environmental-tape-archiveand-library-petal/) and are available upon request to JMCP.

Appendix A. Supplementary data

Supplementary data to this article can be found online at https://doi.org/10.1016/j.icarus.2019.113395.

References

Ade, P.A.R., et al., 2014. Planck 2013 results. XIV. Zodiacal emission. Astron. Astrophys. 571, 25.

Adolfsson, L.G., Gustafson, B.A.S., Murray, C.D., 1996. The Martian atmosphere as a meteoroid detector. Icarus 119, 144–152.

Anders, E., 1989. Pre-biotic organic matter from comets and asteroids. Nature 342, 255.

Andersson, L., et al., 2015. Dust observations at orbital altitudes surrounding Mars. Science 350, 3.

Arndt, P., Bohsung, J., Maetz, M., Jessberger, E.K., 1996. The elemental abundances in interplanetary dust particles. Meteor. Planet. Sci. 31, 817–833.

Benna, M., Mahaffy, P.R., Grebowsky, J.M., Fox, J.L., Yelle, R.V., Jakosky, B.M., 2015a. First measurements of composition and dynamics of the Martian ionosphere by MAVEN's neutral gas and ion mass spectrometer. Geophys. Res. Lett. 42, 8958–8965.

Benna, M., Mahaffy, P.R., Grebowsky, J.M., Plane, J.M.C., Yelle, R.V., Jakosky, B.M., 2015b. Metallic ions in the upper atmosphere of Mars from the passage of comet C/2013 A1 (siding spring). Geophys. Res. Lett. 42, 4670–4675.

Benner, S.A., Devine, K.G., Matveeva, L.N., Powell, D.H., 2000. The missing organic molecules on Mars. Proc. Nat. Acad. Sci. 97, 2425–2430.

Biemann, K., et al., 1976. Search for organic and volatile inorganic compounds in surface samples from Chryse-Plantia region of Mars. Science 194, 72–76.

Bones, D.L., Carrillo-Sánchez, J.D., Kulak, A.N., Plane, J.M.C., 2019. Ablation of Meteoritic Ni in the Upper Atmosphere: Experimental and Computer Simulations and Implications for Fe Ablation. (Under review).

Borin, P., Cremonese, G., Marzari, F., Lucchetti, A., 2017. Asteroidal and cometary dust flux in the inner solar system. Astron. Astrophys. 605, 12.

Brooke, J.S.A., et al., 2017. Meteoric smoke deposition in the polar regions: a comparison of measurements with global atmospheric models. J. Geophys. Res.-Atmos. 122, 11112–11130.

Bullock, E.S., Gounelle, M., Lauretta, D.S., Grady, M.M., Russell, S.S., 2005. Mineralogy and texture of Fe-Ni sulfides in CI1 chondrites: clues to the extent of aqueous alteration on the CI1 parent body. Geochim. Cosmochim. Acta 69, 2687–2700.

Burgess, R., Wright, I.P., Pillinger, C.T., 1991. Determination of sulfur-bearing components in C1 and C2 carbonaceous chondrites by stepped combustion. Meteoritics 26, 55–64.

Carrillo-Sánchez, J.D., Plane, J.M.C., Feng, W., Nesvorny, D., Janches, D., 2015. On the size and velocity distribution of cosmic dust particles entering the atmosphere. Geophys. Res. Lett. 42, 6518–6525.

Carrillo-Sánchez, J.D., Nesvorny, D., Pokorny, P., Janches, D., Plane, J.M.C., 2016. Sources of cosmic dust in the Earth's atmosphere. Geophys. Res. Lett. 43, 11979–11986.

Chase, M.W., Davies, C.A., Downey Jr., J.R., Frurip, D.J., McDonald, R.A., Syverud, A.N., 1985. JANAF thermodynamic tables. J. Phys. Chem. Ref. Data 14 (Suppl. 1, pages 1174-1179), 1621–1625 (Michigan (U.S.A.).

Chyba, C., Sagan, C., 1992. Endogenous production, exogenous delivery and impact-shock synthesis of organic-molecules - an inventory for the origins of life. Nature 355, 125–132.

Clarke, R.S.J., Jarosewich, E., Mason, B., Nelem, J., Gómez, M., Hyde, J.R., 1971. The Allende, Mexico, meteorite shower. The Smithsonian Contributions to the Earth Sciences 5, 45 (Washington).

Collins, R.L., M., J.,L., C, M., 2015. First lidar observation of the mesospheric nickel layer. Geophys. Res. Lett. 42, 665–671.

Conard, B.R., McAneney, T.B., Sridhar, R., 1978. Thermodynamics of Iron-nickel alloys by mass spectrometry. Metallurg. Trans. B-Process Metallurgy. 9, 463–468.

Consolmagno, G.J., Britt, D.T., Macke, R.J., 2008. The significance of meteorite density and porosity. Chemie Der Erde-Geochemistry 68, 1–29.

Crismani, M.M.J., et al., 2017. Detection of a persistent meteoric metal layer in the Martian atmosphere. Nat. Geosci. 10, 401–404.

Cziczo, D.J., Thomson, D.S., Murphy, D.M., 2001. Ablation, flux, and atmospheric implications of meteors inferred from stratospheric aerosol. Science 291, 1772–1775.

Duft, D., Nachbar, M., Leisner, T., 2018. Unravelling the microphysics of polar mesospheric cloud formation. Atmos. Chem. Phys. Discuss. https://doi.org/10.5194/acp-2018-1018.

Endress, M., Zinner, E., Bischoff, A., 1996. Early aqueous activity on primitive meteorite parent bodies. Nature 379, 701.

Fegley, B.J., Cameron, A.G.W., 1987. A vaporization model for Iron silicate fractionation in the Mercury protoplanet. Earth Planet. Sci. Lett. 82, 207–222.

Fixsen, D.J., Dwek, E., 2002. The zodiacal emission spectrum as determined by COBE and its implications. Astrophys. J. 578, 1009.

Flynn, G.J., 1991. The Environmental Model of Mars. Pergamon Press PLC, London.

Flynn, G.J., 1996. The delivery of organic matter from asteroids and comets to the early surface of Mars. Earth Moon Planets 72, 469–474.

Flynn, G.J., McKay, D.S., 1990. An assessment of the meteoritic contribution to the Martian soil. J. Geophys. Res.-Solid Earth and Planets. 95, 14497–14509.

Flynn, G.J., Bajt, S., Sutton, S.R., Zolensky, M.E., Thomas, K.L., Keller, L.P., 1996. The Abundance Pattern of Elements Having Low Nebular Condensation Temperatures in Interplanetary Dust Particles: Evidence for a New Chemical Type of Chondritic Material. Astronomical Soc Pacific, San Francisco.

Flynn, G.J., Keller, L.P., Feser, M., Wirick, S., Jacobsen, C., 2003. The origin of organic matter in the solar system: evidence from the interplanetary dust particles. Geochim. Cosmochim. Acta 67, 4791–4806.

Frankland, V.L., James, A.D., Carrillo-Sánchez, J.D., Nesvorný, D., Pokorný, P., Plane, J.M.C., 2017. CO oxidation and O_2 removal on meteoric material in Venus' atmosphere. Icarus 296, 150–162.

Fredriksson, K., Kerridge, J.F., 1988. Carbonates and sulfates in CI chondrites - formation by aqueous acitivity on the parent body. Meteoritics 23, 35–44.

Gardner, C.S., Liu, A.Z., Marsh, D.R., Feng, W.H., Plane, J.M.C., 2014. Inferring the global cosmic dust influx to the Earth's atmosphere from lidar observations of the vertical flux of mesospheric Na. J. Geophys. Res.-Space Physics. 119, 10.

Gerding, M., Saly, S., Plane, J.M.C., 2018. Lidar soundings of the mesospheric nickel layer using Ni(^{3}F) and Ni(^{3}D) transitions. Geophys. Res. Lett. 46, 408–415.

Gómez Martín, J.C., Brooke, J.S.A., Feng, W., Höpfner, M., Mills, M.J., Plane, J.M.C., 2017. Impacts of meteoric sulfur in the Earth's atmosphere. J. Geophys. Res.-Atmos. 122, 7678–7701.

Gómez-Martín, J. C., et al., 2017. Novel experimental simulations of the atmospheric injection of meteoric metals. Astrophys. J. 836, art. no.: 212.

Gordon, P.R., Sephton, M.A., 2016. Organic matter detection on Mars by pyrolysis-FTIR: an analysis of sensitivity and mineral matrix effects. Astrobiology 16, 831–845.

Grebowsky, J.M., Goldberg, R.A., Pesnell, W.D., 1998. Do meteor showers significantly perturb the ionosphere? J. Atmos. Solar-Terr. Phys. 60, 607–615.

Grebowsky, J.M., Benna, M., Plane, J.M.C., Collinson, G.A., Mahaffy, P.R., Jakosky, B.M., 2017. Unique, non-earthlike, meteoritic ion behavior in upper atmosphere of Mars. Geophys. Res. Lett. 44, 3066–3072.

Greshake, A., et al., 1998. Heating experiments simulating atmospheric entry heating of micrometeorites: clues to their parent body sources. Meteorit. Planet. Sci. 33, 267–290.

Grün, E., Zook, H.A., Fechtig, H., Giese, R.H., 1985. Collisional balance of the meteoritic complex. Icarus 62, 244–272.

Hayatsu, R., Matsuoka, S., Scott, R.G., Studier, M.H., Anders, E., 1977. Origin of organic matter in early solar system: 7. Organic polymer in carbonaceous chondrites. Geochim. Cosmochim. Acta 41, 1325–1339.

Hayatsu, R., Winans, R.E., Scott, R.G., McBeth, R.L., Moore, L.P., Studier, M.H., 1980. Phenolic ethers in the organics polymer of the Murchinson meteorite. Science 207, 1202–**1204**.

Hedin, A.E., 1991. Extension of the MSIS thermosphere model into the middle and lower atmosphere. J. Geophys. Res. 96, 1159–1172.

Hughes, 1978. Meteors. In: McDonnell, J.A.M. (Ed.), Cosmic Dust. Wiley, London, UK, pp. 123–185.

Hutchinson, R., 2004. Meteorites: A Petrologic, Chemical and Isotopic Synthesis.

Jarosewich, E., 1990. Chemical-analyses of meteorites: a compilation of stony and iron meteorite analyses. Meteoritics 25, 323–337.

Jessberger, E.K., Christoforidis, A., Kissel, J., 1988. Aspects of the major element composition of Halley's dust. Nature 332, 691–695.

Kane, T.J., Gardner, C.S., 1993. Lidar observations of the meteoric deposition of mesospheric metals. Science 259, 1297–1300.

Keating, G.M., et al., 1985. Models of Venus neutral upper atmosphere: structure and composition. Adv. Space Res. 5, 117–171.

Kliore, A.J., Patel, I.R., Nagy, A.F., Cravens, T.E., Gombosi, T.I., 1979. Initial obervations of the nightside ionosphere of Venus from Pioneer Venus orbiter radio occultations. Science 205, 99–102.

Kopp, E., 1997. On the abundance of metal ions in the lower ionosphere. J. Geophys. Res.-Space Phys. 102, 9667–9674.

Levin, G.V., Straat, P.A., 1979a. Completion of the Viking labeled release experiment on Mars. J. Molec. Evol. 14, 167–183.

Levin, G.V., Straat, P.A., 1979b. Viking Mars labeled release results. Nature 277, 326.

Lewis, J.M.T., Watson, J.S., Najorka, J., Luong, D., Sephton, M.A., 2015. Sulfate minerals: a problem for the detection of organic compounds on Mars? Astrobiology 15, 247–258.

Lewis, S.R., et al., 1999. A climate database for Mars. J. Geophys. Res.-Planets. 104, 24177–24194.

Lodders, K., Fegley, B.J., 2011. Chemistry of the Solar System. The Royal Society of Chemistry, Cambridge, UK.

Loes ten Kate, I., 2018. Organic molecules on Mars. Science 360, 1068–1069.

Mahaffy, P.R., et al., 2015a. Structure and composition of the neutral upper atmosphere of Mars from the MAVEN NGIMS investigation. Geophys. Res. Lett. 42, 8951–8957.

Mahaffy, P.R., et al., 2015b. The neutral gas and ion mass spectrometer on the Mars atmosphere and volatile evolution mission. Space Sci. Rev. 195, 49–73.

McKay, D.S., et al., 1996. Search for past life on Mars: possible relic biogenic activity in Martian meteorite ALH84001. Science 273, 924–930.

Moorhead, A.V., Wiegert, P.A., Cooke, W.J., 2014. The meteoroid fluence at Mars due to comet C/2013 A1 (siding spring). Icarus 231, 13–21.

Nesvorný, D., Vokrouhlicky, D., Bottke, W.F., Sykes, M., 2006. Physical properties of asteroid dust bands and their sources. Icarus 181, 107–144.

Nesvorný, D., Jenniskens, P., Levison, H.F., Bottke, W.F., Vokrouhlický, D., Gounelle, M., 2010. Cometary origin of the zodiacal cloud and carbonaceous micrometeorites. Implications for hot debris disks. Astrophys. J. 713, 816–836.

Nesvorný, D., Janches, D., Vokrouhlický, D., Pokorný, P., Bottke, W.F., Jenniskens, P., 2011. Dynamical model for the zodiacal cloud and sporadic meteors. Astrophys. J. 743 (2), 129–144.

Noguchi, T., et al., 2015. Cometary dust in Antarctic ice and snow: past and present chondritic porous micrometeorites preserved on the Earth's surface. Earth Planet. Sci. Lett. 410, 1–11.

Orofino, V., Blanco, A., Blecka, M.I., Fonti, S., Jurewicz, A., 2000. Carbonates and coated particles on Mars. Planet. Space Sci. 48, 1341–1347.

Paetzold, M., et al., 2009. A sporadic layer in the Venus lower ionosphere of meteoric origin Geophys. Res. Lett. 36, art. no.: L05203.

Palomba, E., Zinzi, A., Clouds, E.A., D'Amore, M., Grassi, D., Maturilli, A., 2009. Evidence for Mg-rich carbonates on Mars from a 3.9 mu m absorption feature. Icarus 203, 58–65.

Pellinen-Wannberg, A.K., Haggstrom, I., Carrillo-Sánchez, J.D., Plane, J.M.C., Westman, A., 2014. Strong E region ionization caused by the 1767 trail during the 2002

Leonids. J. Geophys. Res.-Space Phys. 119, 7880–7888.
Plane, J.M.C., 2003. Atmospheric chemistry of meteoric metals. Chem. Rev. 103, 4963–4984.
Plane, J.M.C., Feng, W., Dawkins, E.C.M., 2015. The mesosphere and metals: chemistry and changes. Chem. Rev. 115, 4497–4541.
Plane, J.M.C., Carrillo-Sanchez, J.D., Mangan, T.P., Crismani, M.M.J., Schneider, N.M., Maattanen, A., 2018. Meteoric metal chemistry in the Martian atmosphere. J. Geophys. Res.-Planets. 123, 695–707.
Pokorný, P., Vokrouhlický, D., Nesvorný, D., Campbell-Brown, M., Brown, P., 2014. Dynamical model for the toroidal sporadic meteors. Astrophys. J. 789, art. no.: 25.
Reach, W.T., 1988. Zodiacal emission .1. Dust near the Earth's orbit. Astrophys. J. 335, 468–485.
Reach, W.T., 1992. Zodiacal emission .3. Dust near the Asteroid Belt. Astrophys. J. 392, 289–299.
Reach, W.T., Franz, B.A., Weiland, J.L., 1997. The three-dimensional structure of the zodiacal dust bands. Icarus 127, 461–484.
Rietmeijer, F.J.M., 2009. A cometary aggregate interplanetary dust particle as an analog for comet wild 2 grain chemistry preserved in silica-rich stardust glass. Meteorit. Planet. Sci. 44, 1589–1609.
Rowan-Robinson, M., May, B., 2013. An improved model for the infrared emission from the zodiacal dust cloud: cometary, asteroidal and interstellar dust. Mon. Not. Roy. Astron. Soc. 429, 2894–2902.
Schaefer, L., Fegley, B., 2004. A thermodynamic model of high temperature lava vaporization on Io. Icarus 169, 216–241.
Schneider, N.M., et al., 2015. MAVEN IUVS observations of the aftermath of the comet siding spring meteor shower on Mars. Geophys. Res. Lett. 42, 4755–4761.
Sephton, M.A., Botta, O., 2008. Extraterrestrial organic matter and the detection of life. Space Sci. Rev. 135, 25–35.
Sephton, M.A., Wright, I.P., Gilmour, I., de Leeuw, J.W., Grady, M.M., Pillinger, C.T., 2002. High molecular weight organic matter in martian meteorites. Planet. Space Sci. 50, 711–716.
Stenzel, O.J., et al., 2017. Similarities in element content between comet 67P/Churyumov–Gerasimenko coma dust and selected meteorite samples. Mon. Not. Roy. Astron. Soc. 469, S492–S505.
Subasinghe, D., Campbell-Brown, M.D., Stokan, E., 2016. Physical characteristics of faint meteors by light curve and high-resolution observations, and the implications for parent bodies. Mon. Not. Roy. Astron. Soc. 457, 1289–1298.
Swartzendruber, L.J., Itkin, V.P., Alcock, C.B., 1991. The Fe-Ni (iron-nickel) system. J. Phase Equil. 12, 288–312.
Taylor, S., Lever, J.H., Harvey, R.P., 1998. Accretion rate of cosmic spherules measured at the south pole. Nature 392, 899–903.
Vondrak, T., Plane, J.M.C., Broadley, S., Janches, D., 2008. A chemical model of meteoric ablation. Atmos. Chem. Phys. 8, 7015–7031.
Walder, P., Pelton, A.D., 2005. Thermodynamic modeling of the Fe-S system. J. Phase Equil. Diff. 26, 23–38.
Waldner, P., Pelton, A.D., 2004. Critical thermodynamic assessment and modeling of the Fe-Ni-S system. Metallurg. Mater. Trans. B. 35, 897–907.
Whalley, C.L., Plane, J.M.C., 2010. Meteoric ion layers in the Martian atmosphere. Faraday Discuss. 147, 349–368.
Yang, H. G., Ishiguro, M., 2015. Origin of interplanetary dust through optical properties of the zodiacal light. Astrophys. J. 813, art. no.: 87.
Yen, A. S., et al., 2006. Nickel on Mars: constraints on meteoritic material at the surface. J. Geophys. Res.-Planets. 111, art. no.: E12S11.
Zolensky, M.E., Bourcier, W.L., Gooding, J.L., 1989. Aqueous alteration on the hydrous asteroids: results of EQ3/6 computer simulations. Icarus 78, 411–425.
Zook, H.A., 2001. Spacecraft measurements of the cosmic dust flux. In: Peucker-Ehrenbrink, B., Schmitz, B. (Eds.), Accretion of Extraterrestrial Matter throughout Earth's History. Springer US, Boston, MA, pp. 75–92.